Stony Brook University

OFFICIAL COPY

The official electronic file of this thesis or dissertation is maintained by the University Libraries on behalf of The Graduate School at Stony Brook University.

© All Rights Reserved by Author.

Turbulent Mixing in Richtmyer-Meshkov Instability Using Front-Tracking

A Dissertation Presented

by

Pooja Rao

to

The Graduate School

In Partial Fulfillment of the

Requirements

for the Degree of

Doctor of Philosophy

in

Applied Mathematics and Statistics

Stony Brook University

August 2016

Stony Brook University

The Graduate School

Pooja Rao

We, the dissertation committee for the above candidate for the
Doctor of Philosophy degree, hereby recommend
acceptance of this dissertation.

James Glimm - Dissertation Advisor
Distinguished Professor, Department of Applied Mathematics and Statistics

Xiangmin Jiao - Chairperson of Defense
Associate Professor, Department of Applied Mathematics and Statistics

Xiaolin Li - Member
Professor, Department of Applied Mathematics and Statistics

Michael McGuigan - Outside Member
Deputy Director, Computational Scientist, Brookhaven National Lab

This dissertation is accepted by the Graduate School.

Charles Taber
Dean of the Graduate School

Abstract of the Dissertation

Turbulent Mixing in Richtmyer-Meshkov Instability Using Front-Tracking

by

Pooja Rao

Doctor of Philosophy

in

Applied Mathematics and Statistics

Stony Brook University

2016

Turbulent mixing from hydrodynamical instabilities, such as Richtmyer-Meshkov (RMI) and Rayleigh-Taylor (RTI) instabilities, plays a critical role in numerous applications ranging from performance degradation in inertial confinement capsules to supernova explosions. At high Reynolds numbers (Re), for which experimental data is not available, numerical simulations are paramount in studying these instabilities. However, the algorithmic differences due to differences in numerical modeling often give solutions that are converged but not unique, that is, different codes converge to different solutions. Thus, to establish the credibility of the simulation in an objective manner, it is necessary to fulfill three main requirements: (1) verification (2) validation and (3) uncertainty quantification.

In this dissertation, we present a "validation by extrapolation" strategy accompanied with appropriate interface and subgrid modeling. Instead of us-

ing the traditional pointwise convergence, we use Youngs' measure, which is stochastic in nature and is more appropriate for studying turbulent properties. We also analyze the stochastic properties of turbulence using exponential distribution across Re and mesh.

The highlight of our numerical algorithm is use of front-tracking in conjunction with dynamic subgrid scale models. This unique combination has been successfully verified for RMI and validated for RTI. The use of front-tracking and a calibration-free SGS model facilitates the smooth extrapolation of LES simulations from experimentally validated regime to higher Re. This seamless extrapolation is important in designing simulations that are truly predictive in nature.

Motivated by the Richtmyer-Meshkov instability in inertial confinement fusion, we carry out a parameter study on a simplified hydrodynamical version of the ICF problem in 2D. In this parameter study, we vary the Reynolds number starting from the experimentally achieved highest Re for RTI $(35,000)$ to $Re = \infty$ (Euler's equation/no physical viscosity). At such high Re, turbulent transport is the dominant mode of transport. We analyze the sensitivity of the turbulent transport coefficients (calculated via the dynamic SGS) to the Reynolds number. These coefficients vary little in the high Re range. However, they are observed to be very sensitive to the changes in subgrid model, thus emphasizing the importance of using the parameter-free subgrid models for turbulent mixing problems.

We find that in high Re limit, the turbulent transport coefficients are converged under mesh refinement and have a Kolmogorov-type scaling. We also

draw quantitative comparisons between the single-shocked incipiently turbulent regime and the reshocked regime with fully developed turbulence.

To my little nephews, Arjun and Aryan, who have been a constant source of joy in my life since the day they were born.

Table of Contents

List of Figures

List of Tables

Acknowledgments

First and foremost, I express my sincere gratitude to my Ph.D. advisor Dr. James Glimm for his support and guidance throughout my time at Stony Brook. His scientific advice and knowledge have been very valuable and he will continue to be a role model in my future scientific endeavors.

I also want to thank Dr. Xiangmin Jiao, Dr. Xiaolin Li and Dr. Mike McGuigan for being on the dissertation committee and for their insightful questions and comments.

I had the pleasure to work with Dr. Hyunkyung Lim, Dr. Jeremy Melvin, Dan She, Dr. Ryan Kaufman, Abigail Hsu and others from the research group at Stony Brook. The interactions with them have helped me grow as a researcher and as a person. A special thanks to Dr. Jeremy Melvin, who has been a very helpful project partner and a good friend. I have benefited tremendously from our discussions.

I am also appreciative of the opportunity to attend the Mathematics of Turbulence Program at IPAM, UCLA, where I got to work closely with Dr. John Gibbon and Dr. C.P. Caulfield. I learned a lot from working with these two exceptional scientists.

I thank Dr. Prabhat and Dr. Karthik Kashinath at Lawrence Berkeley National Lab, with whom I had the opportunity to work in the exciting area of climate science.

I want to thank all my friends for their love and support. A special thanks to my grandparents, Bhu Yadav and Dr. J.N.S. Yadav, for being a source of inspiration and love. Last but not the least, I would like to thank my parents, Dr. Krishna Yadav and R.K. Yadav, sister-in-law Bharti Singh Rao, brother Yatin Rao and my nephews, Arjun Rao and Aryan Rao, for their unconditional love and encouragement. This accomplishment could not have been possible without them.

Chapter 1

Introduction

1.1 Overview

Turbulent mixing [43, 9] from hydrodynamical instabilities, such as Rayleigh-Taylor instability (RTI) [37, 51, 15] and Richtmyer-Meshkov instability (RMI) [42, 4, 5], plays a critical role in numerous engineering as well as natural applications. The experimental data at such extreme conditions is either not available or is very limited, i.e., only few quantities can be measured directly and those measurements may have large errors. In such a scenario, one of the most important tools to study mixing is numerical simulations. However, they come with their own set of challenges [46]. As the Re increases, the number of physical scales also increases and it becomes more computationally expensive to simulate the problem.

Additionally, the solutions obtained from these simulations may not converge or may not converge to the right solution. On top of that code com-

parison is hard as algorithmic differences among codes make them converge to different solutions and thus, different quantities of mix is obtained using different codes [8]. Numerical diffusion plays an important part in it as it alters the dynamics of the problem and leads to unphysical mixing. Thus, to establish the credibility of the simulation in an objective manner, it is necessary to fulfill three main requirements: (1) verification (2) validation and (3) uncertainty quantification [45, 31].

In this dissertation, we mitigate numerical diffusion by utilizing Front-tracking (FT) to evolve the contact discontinuity. At high Reynolds number (Re), the dissipation from small scales is important and is modeled using the dynamic subgrid scale model (SGS) from Germano [13]. Based on this unique combination that has been validated extensively for a similar class of problems at lower Re, we suggest a "validation by extrapolation" strategy to design simulations that are predictive in the extended Re regime.

The use of Front-tracking and a calibration-free SGS model facilitates the smooth extrapolation of large eddy simulations (LES) from the experimentally validated regime to higher Re. This seamless extrapolation is important in designing simulations that are truly predictive in nature.

One of the important charateristic of turbulence is its irregular and random nature, requiring statistical methods to study it. Instead of using pointwise convergence, we use the idea of stochastic convergence which is more suitable for such flows. Together, they form a verification and validation (V&V) strategy for designing robust LES simulations. We also analyze the stochastic properties of turbulence by fitting an exponential distribution to the front

crossings.

1.2 Turbulence and Large Eddy Simulations

The Navier-Stokes equations are considered an accurate representation of the turbulent fluid flow. The dimensionless parameter that is used to characterize the intensity of turbulence is the Reynolds number given by:

$$Re = \frac{UL}{\nu} \tag{1.1}$$

where U, L are the characteristic velocity and length and ν is the kinematic viscosity.

Among the many scales of turbulence, the largest scales are more dependant on the geometry of the specific problem and contain most of the energy of the system, while the small scales are thought to be more universal and dissipative in nature. For computational purposes, it is not always possible to compute all the scales numerically. Often, a filter operation is applied on the governing equations to separate the small scales from the large ones. Direct Numerical Simulation (DNS) attempts to simulate all the scales of turbulence up to the Kolmogorov scale. It is very accurate, but is really expensive and only feasible for low to moderate Re ($\sim O(10,000)$). LES computes the big scales and models the small scales (known as the subgrid scales).

For most scientific or engineering applications, DNS is not feasible. For example, Reynolds number characterizing mixing in supernova explosions is estimated to be of order 10^{10} [50]. At such high Re, LES is paramount in

studying the turbulent mixing.

The subgrid scales (SGS) in LES are a source of dissipation. If the subgrid dissipation is treated explicitly using some appropriate theoretical/physical model, we refer to those simulations simply as LES. In the implicit LES (ILES), numerical diffusion is used as a proxy for subgrid dissipation [53]. It may be a little risky as unlike subgrid models, it is hard to quantify how much numerical diffusion there is in the problem compared to actual subgrid diffusion.

However, on Eulerian grids that are not finely resolved, using explicit SGS without any appropriate interface modeling can add excess diffusion to the problem and thus, affect the amount of mix. For the class of problems that we are interested in studying, the presence of a contact discontinuity places a refinement requirement that may be very restrictive/infeasible for high Re. For such problems, Front-tracking (FT) provides a very accurate and computationally reasonable tool.

The highlight of our numerical algorithm (FT/LES/SGS) is the use of Front-tracking in conjunction with dynamic subgrid scale models. This unique combination has been sucessfully verified for RMI and validated for RTI. Front-tracking propagates the contact discontinuity in a Lagrangian fashion by solving a Riemann problem across it. As a result, the interface is sharp, even for coarser grids, and it mitigates the problem of numerical diffusion across the jump discontinuity. The dynamic subgrid model developed by Germano captures the effect of the unresolved scales using the local flow conditions, thus eliminating the need for tunable parameters in the LES simulations. The use of calibration-free dynamic subgrid model along with appropriate interface

tracking is the key to designing predictive simulations at high Re.

1.2.1 Hydrodynamical Instabilities

Rayleigh-Taylor instability (RTI) is a hydrodynamical instability that occurs when the light fluid accelerates the heavy fluid in presence of a continuous acceleration [48, 37]. The initial perturbations follow an exponential growth. Richtmyer-Meshkov instability (RMI) is another hydro instability that is closely related with RTI. It is a limiting case of RTI in the sense that it is driven by impulsive acceleration instead of continuous acceleration. It was first studied theoretically by Richtmyer [49] and its existence was confirmed experimentally via the shock tube experiments of Meshkov [42]. It occurs when a shock wave (impulsive acceleration) passes through the density discontinuity at the perturbed interface betwen the two fluids. The shock wave can be generated by an instantaneous pressure gradient and the fluid interface provides the density gradient. The misalignment between the pressure and density gradients ($\nabla p \cdot \nabla \rho$) deposits the voricity at the interface, which drives the instability and amplifies the initial perturbations.

RTI occurs only when the light fluid is accelerating the heavy fluid. Unlike RTI, there are two possible configurations for planar RMI:

- light fluid accelerating the heavy
- heavy fluid accelerating the light

A lot of applications in RMI (to be discussed in the next section) occur in circular geometry. With circular geometry, the shock wave can travel inwards

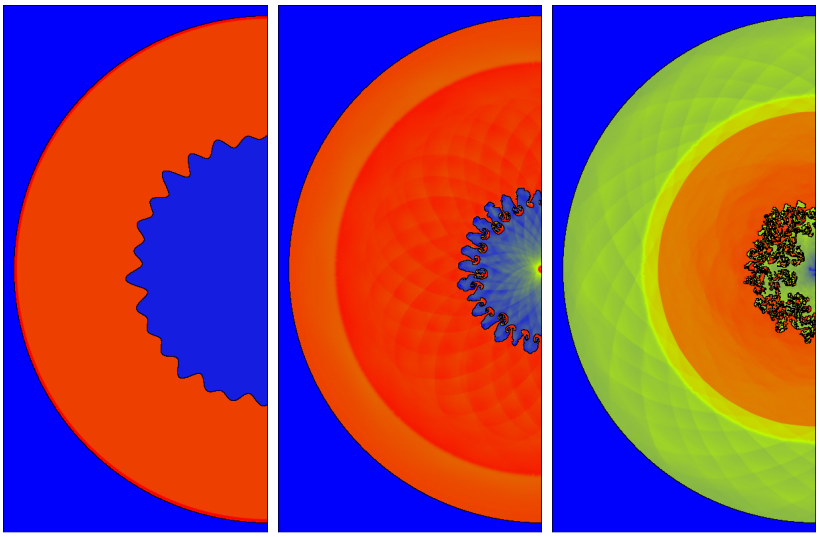

Figure 1.1: Richtmyer-Meshkov instability in circular geometry taken from our 2D simulations. **Left:** Initial time **Center:** After shock **Right:** After reshock

or outwards, which adds to the number of possible configurations:

- light fluid imploding the heavy
- light fluid exploding the heavy
- heavy fluid imploding the light
- heavy fluid exploding the light

The growth of the fluid interface (Fig. 1.1) can be thought of as a four stage process:

1. Initial linear growth
2. Non-linear growth that results in formation of spikes (heavy fluid entering the light fluid) and bubbles (light fluid penetrating the heavy fluid)

3. Development of secondary instabilities like Kelvin-Helmholtz and formation of mushroom like structures

4. Transformation into a fully developed turbulent mixing zone via breaking of large scale coherent structures into small scale structures. This stage is reached at sufficiently late time/in presence of reshock.

The growth in the RMI is inherently asymmetrical as the spikes grow faster than the bubbles. This difference in growth is attributed to At (Atwood number),

$$At = \frac{\rho_h - \rho_l}{\rho_h + \rho_l} \tag{1.2}$$

which characterizes the density difference between the two fluids. The higher the At number, the bigger the density difference and thus, a larger discrepancy in the bubble and spike growth.

In this disseration, we are going to study the case (heavy fluid imploding the light) that corresponds to the setup in the inertial confinement fusion (ICF) capsule, which will be discussed later in the section. For planar and circular geometries, the basic physics of the instability is the same. However, the imploding circular geometry allows the shock to bounce off the reflecting boundaries and reshock the interface. This gives rise to stronger mixing.

1.3 Applications

Turbulent mixing from hydrodynamical instabilities, such as RMI and RTI, plays a critical role in numerous engineering as well as natural applications

[26, 41, 24]. In scramjet engine, a rapid mixing of the fuel and the oxidizer is required due to limited time and space available in the chemical combustor [21]. The turbulent mixing induced by RMI enhances the overall mixing process and is benefical to the performace of the engine.

In supernova explosions, the heavy elements like iron that are produced in the core of the star are found in the outer regions of the core. The outward propagating shock wave generated by the collapsing star and the density difference among different stellar layers cause the RMI to occur, which results in turbulent mixing and transport of the material between layers [28, 10].

Inertial confinement fusion is an approach to fusion that relies on the inertia of fuel mass to provide confinement [35, 22, 36, 39]. In ICF, laser beams or laser produced x-rays heat the surface of the fusion target, a spherical pellet containing Deuterium-Tritium (DT)-gas surrounded by denser but colder DT-ice. The energy from the driver causes the surface of the pellet to ablate and to counter this motion, the rest of the target is driven inwards. This compresses the core giving rise to very high temperature and pressure, and results in thermonuclear burn. The burn propagates outwards at a speed faster than at which the fluids expand outwards and thus contains the fluid. The biggest challenge to achieve thermonuclear fusion is confining plasma at the temperature and density conditions required by a particular species to overcome the Coulomb repulsion force.

The RM instability in ICF causes the pre-mature mixing of the capsule material with the fuel, limiting the compression of the fuel and affects the energy production. Therefore, assessing the mixing caused by this instability

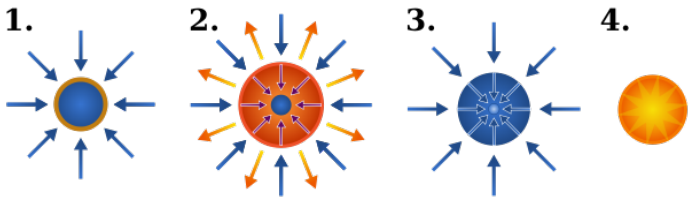

Figure 1.2: A cartoon of the ICF capsule depicting the various stages of the compression of the capsule that ultimately results in nuclear fusion (en.wikipedia.org/wiki/Inertial_confinement_fusion).

is critical for the performance of the experiment.

Motivated by the Richtmyer-Meshkov instability in ICF, we carry out a parameter study on a simplified hydrodynamical version of the ICF problem in 2D. In this parameter study, we vary the Reynolds number starting from the experimentally achieved highest Re for RTI (35000) to $Re = \infty$ (Euler's equation/no physical viscosity). At such high Re, turbulent trasnport is the dominant mode of transport. We analyze the sensitivity of the turbulent trasnport coefficients (calculated via the dynamic SGS) to the Reynolds number. These coefficients vary little in the high Re range. However, they are observed to be very sensitive to the changes in subgrid model, thus emphasizing the importance of using the appropriate subgrid models for turbulent mixing problems.

We find that in the high Re limit, the turbulent transport coefficients are converged under mesh refinement and have a Kolmogorov-type scaling. We also draw quantitative comparisons between the single-shocked incipiently turbulent regime and the reshocked regime with fully developed turbulence.

1.4 Outline

In Chapter 2, we talk about the governing equations and the details of our numerical method (FT/LES/SGS). We also talk about the tool W-star that uses the concept of a Youngs' measure to study the convergence.

Chapter 3 and 4 contain the results from our study on a hydrodynamical toy problem in 2D mimicing an inertial confinement capsule. In section 1 of Chapter 3, we give the values of the parameters used in the simulation. We discuss mixing in terms of concentration and temperature and document their sensitivity to change in subgrid parameters. We analyze the concentration data by fitting it to beta distribution.

In Chapter 4, we look at the subgrid coefficients more closely. We study them under mesh refinement and under increase of Re. We report Kolmogorov-type scaling for these coefficients.

In chapter 5, we present results from our investigation of the spatial distribution of mixing by fitting an exponential distrbution to the front crossings.

In Chapter 6, we present conclusions from our study.

Chapter 2

Methods and Tools

The main feature of our numerical algorithm is the use of Front-tracking and a dynamic subgrid scale model for the LES simulations (FT/LES/SGS). This unique algorithm is calibration-free and thus, easier to extend from validation range ($Re = 35 \times 10^3$). In this chapter, we will give an overview of each of these methods.

Front-tracking is used only for the interface points and the rest of the grid points are solved using a regular Eulerian numerical solver. For the simulations under study here, we have used the in-house Front-tracking code FronTier enhanced with SGS. FronTier uses finite volume scheme MUSCL (Monotonic Upstream centered Scheme for Conservation Laws) to compute solution on the rest of the grid points away from the front points.

2.1 Governing Equations

As discussed in the previous chapter, Navier-Stokes are widely regarded as an accurate mathematical representation of the turbulent flows. We use these equations as our governing system of equations.

In light of our high Re parameter study, we use LES approach [33] to numerically simulate the flow. It has good accuracy without being computationally too expensive. As the name suggests, it seeks to predict the motion of the largest and most important eddies, which are supposed to be uncoupled from the small eddies. This is based on the fact that the largest eddies carry most of the energy and should be resolved, while the mostly dissipative small scales are more universal in character and thus, easier to model.

The application of LES can be broken down into three steps:

1. The first step is to apply a low pass filter on the Navier-Stokes equations to remove the small spatial scales or fluctuations, but retain the bigger more important scales.

   The grid filter used in our code is simply the average over the cell values. This type of filtering is called implicit filtering and is commonly used for finite volume codes.

   The resulting equations that describe the space-time evolution of large eddies contain subgrid terms that describe the effect of unresolved small scales on the resolved scales. With the addition of these subgrid terms, there are more unknowns than equations.

2. The second step is the calculation of the unresolved or "subgrid" terms

by a model that uses the information contained in the resolved scales effectively to calculate these terms.

3. The last step is the numerical simulation of the resulting closed equations for the large scale fields.

2.2 Dynamic Subgrid Scale Model

The turbulent transport is the dominant transport mechanism in the high Re range that we are interested in studying. It is defined in terms of the transport coefficients:

- turbulent anisotropic viscosity
- turbulent isotropic viscosity
- turbulent species mass diffusion
- turbulent thermal diffusion

These terms are calculated using SGS. The subgrid model used for running our simulations is a dynamic subgrid scale model. It was developed by Germano for incompressible flows and extended to compressible flows by Moin [13, 44]. It is based on Smagorinsky's eddy viscosity model [52] and has been highly successful.

The original model proposed by Smagorinsky used the idea of eddy viscosity:

$$\nu_t = C_S \Delta^2 \mid \widetilde{S} \mid \tag{2.1}$$

where ν_t is the eddy viscosity, Δ represents the grid spacing, C_s is the model coefficient and S is the strain rate tensor defined by

$$S_{ij} = \frac{1}{2}\left(\frac{\partial v_i}{\partial x_j} + \frac{\partial v_j}{\partial x}\right)$$

where v is the velocity.

He obtained the eddy viscosity ν_t, by assuming that at very small scales, the rate of energy production and dissipation are the same. In other words, the small scales are in equilibrium. The small scale were also assumed to be isotropic. Using some of the experiments, he approximated his C_s value to be around 0.23 and it was used as a constant for all the flows. As a result of these assumptions, the model suffered from some limitations like not representing the transient flows and flows near the boundary properly and not accounting for back scatter.

By calculating the coefficients (C_s) dynamically using the local flow conditions, Germano overcame some of the shortcomings. This model is referred to as the dynamic subgrid scale model.

Germano used the Smagorinsky model and applied it at two different levels (grid filter level and test filter level) to calculate the model coefficient C_S dynamically. He assumed that the coefficients values did not depend on the grid level.

Germano found the computed turbulence statistics to be insensitive to the ratio of test filter to the grid filter[13]. For our simulations, we tested a variety of filter sizes and did not find much difference between different filters. We decided to use the test filter that is two times coarser than the grid filter to

be as local as possible.

We demonstrate how SGS is applied on the momentum equation following the filtering operation to obtain the first two turbulent coefficients mentioned above [38, 34]. The rest of the coefficients follow suit.

The momentum equation is expressed as

$$\frac{\partial \rho v_j}{\partial t} + \frac{\partial \rho v_i v_j}{\partial x_i} = -\frac{\partial p \delta_{ij}}{\partial x_i} + \frac{\partial d_{ij}}{\partial x_i} \tag{2.2}$$

where ρ, v, p, d and δ_{ij} represent the density, velocity, pressure, viscous stress tensor and the Kronecker delta function.

The viscous stress tensor d_{ij} from the momentum equation is proportional to the strain rate tensor and the viscosity and is expressed as

$$d_{ij} = v_d \left(\left(\frac{\partial v_i}{\partial x_j} + \frac{\partial v_j}{\partial x_i} \right) - \frac{2}{3} \frac{\partial v_k}{\partial x_k} \delta_{ij} \right) \tag{2.3}$$

where $v_d = \rho v_k$ is the dynamic viscosity. This equation comes from the fact that the momentum transfer caused by the molecular motion in a gas can be described by a molecular viscosity.

On applying the grid filter to the momentum equation, we get

$$\overline{\frac{\partial \rho v_j}{\partial t} + \frac{\partial \rho v_i v_j}{\partial x_i}} = \overline{-\frac{\partial p \delta_{ij}}{\partial x_i} + \frac{\partial d_{ij}}{\partial x_i}} \tag{2.4}$$

$$\Rightarrow \overline{\frac{\partial \rho v_j}{\partial t}} + \overline{\frac{\partial \rho v_i v_j}{\partial x_i}} = \overline{-\frac{\partial p \delta_{ij}}{\partial x_i}} + \overline{\frac{\partial d_{ij}}{\partial x_i}} \tag{2.5}$$

using the commutativity of the averaging operator with differential and addition operator, on regular grids. The Favre averaging for a variable x is defined as :

$$\widetilde{x} = \frac{\overline{\rho x}}{\overline{\rho}}$$

Adding and subtracting the term $\overline{\rho}\widetilde{v_i}\widetilde{v_j}$, rearranging the terms and using Favre averaging to simplify the equation (5), we get :

$$\Rightarrow \frac{\partial \bar{\rho}\tilde{v_j}}{\partial t} + \frac{\partial(\bar{\rho}\tilde{v_i}\tilde{v_j})}{\partial x_i} = \frac{\partial \overline{d_{ij}}}{\partial x_i} - \frac{\partial \bar{\rho}(\widetilde{v_i v_j} - \tilde{v_i}\tilde{v_j})}{\partial x_i} \tag{2.6}$$

$$\Rightarrow \frac{\partial \bar{\rho}\tilde{v_j}}{\partial t} + \frac{\partial(\bar{\rho}\tilde{v_i}\tilde{v_j} + \bar{p}\delta_{ij})}{\partial x_i} = \frac{\partial \overline{d_{ij}}}{\partial x_i} - \frac{\partial \tau_{ij}}{\partial x_i} \tag{2.7}$$

τ_{ij} in (7) is the subgrid stress which is defined as

$$\tau_{ij} = \bar{\rho}(\widetilde{v_i v_j} - \tilde{v_i}\tilde{v_j}) \tag{2.8}$$

It can be rewritten as

$$\tau_{ij} = \underbrace{\left(\tau_{ij} - \tau_{kk}\frac{\delta_{ij}}{3}\right)} + \underbrace{\tau_{kk}\frac{\delta_{ij}}{3}} \tag{2.9}$$

Let τ_{ij}^M denote the model for τ_{ij}, the anisotropic (a) and isotropic parts (i) are modeled separately.

$$\tau_{ij}^M = \tau_{ij}^a + \tau_{ij}^i$$

Applying the same idea as in (3) to turbulent flow, the momentum transfer caused by the turbulent eddies can be modeled with an eddy viscosity. This is known as the eddy viscosity assumption. Using this assumption, the model is given by

$$\tau_{ij}^{M} = -2C_S\Delta^2\bar{\rho} \mid \widetilde{S} \mid \widetilde{S_{ij}^{a}} + \frac{\delta_{ij}}{3}2C_I\Delta^2\bar{\rho} \mid \widetilde{S} \mid^2 \tag{2.10}$$

where $\widetilde{S_{ij}^{a}} = \widetilde{S_{ij}} - \frac{\delta_{ij}}{3}\widetilde{S_{kk}}$ and $\mid S \mid^2 = \sum 2S_{ij}^2$. The C_S and C_I are model coefficients to be computed dynamically.

Using the assumption that the model coefficients are grid independent, we apply the test filter (denoted by hat symbol) on the grid filtered momentum equation. Following the same line of reasoning as used in derivation of sub grid stress at grid filter, the subgrid stress at the test filter level is

$$T_{ij} = \widehat{\overline{\rho v_i v_j}} - \frac{\widehat{\overline{\rho v_i}}\,\widehat{\overline{\rho v_j}}}{\widehat{\bar{\rho}}} \tag{2.11}$$

Writing the anisotropic and isotropic parts separately and modeling, we get

$$T_{ij}^{M} = T_{ij}^{a} + T_{ij}^{i} \tag{2.12}$$

$$T_{ij}^{M} = -2C_S\widehat{\Delta}^2\widehat{\bar{\rho}} \mid \widehat{\widetilde{S}} \mid \widehat{\widetilde{S_{ij}^{a}}} + \frac{2\delta_{ij}}{3}C_I\widehat{\Delta}^2\widehat{\bar{\rho}} \mid \widehat{\widetilde{S}} \mid^2 \tag{2.13}$$

Germano observed that though the subgrid stress at grid filter and test filter levels can't be resolved individually, the difference between these two stresses (filtering the subgrid stress at grid filter using the test filter and subtracting from the subgrid stress at test filter level) is resolvable. This quantity is called the Leonard stress, L_{ij}.

Using Germano's identity, the Leonard stress is

$$L_{ij} = T_{ij} - \widehat{\tau_{ij}} = \widehat{\overline{\rho}\widetilde{v}_i\widetilde{v}_j} - \frac{\widehat{\overline{\rho}\widetilde{v}_i}\widehat{\overline{\rho}\widetilde{v}_j}}{\widehat{\overline{\rho}}} \tag{2.14}$$

which is computable. Using the models for $T_{ij}$and τ_{ij}, we get the modeled anisotropic part of L_{ij} as

$$L^a_{ij} = 2C_S\Delta^2\widehat{\overline{\rho}|\tilde{S}|\tilde{S}^a_{ij}} - 2C_S\widehat{\Delta}^2\widehat{\overline{\rho}} \mid \widehat{\widetilde{S}} \mid \widehat{\widetilde{S}^a_{ij}} = C_S M^a_{ij} \tag{2.15}$$

where $M^a_{ij} = 2\Delta^2\overline{\rho} \mid \widehat{\widetilde{S}} \mid \widehat{\widetilde{S}^a_{ij}} - 2\widehat{\Delta}^2\widehat{\overline{\rho}} \mid \widehat{\widetilde{S}} \mid \widehat{\widetilde{S}^a_{ij}}^a$. The overdetermined system so obtained is solved using the method of least squares.

$$C_S = \frac{< (\sum L^a_{ij}M^a_{ij})^+ >}{< (\sum M^a_{ij}M^a_{ij})^+ >}$$

The expression $(...)^+$ means only the positive part of the quantity is considered.

In a similar manner, the model coefficient C_I is obtained as

$$L^i_{kk} = T^i_{kk} - \widehat{\tau_{kk}}^i = -2C_I\Delta^2\widehat{\overline{\rho} \mid \widetilde{S} \mid^2} + 2C_I\widehat{\Delta}^2\widehat{\overline{\rho}} \mid \widehat{\widetilde{S}} \mid^2 = C_I M^i_{kk}$$

where $M^i_{kk} = -2\Delta^2\widehat{\overline{\rho} \mid \widetilde{S} \mid^2} + 2C_I\widehat{\Delta}^2\widehat{\overline{\rho}} \mid \widehat{\widetilde{S}} \mid^2$

This yields only one equation for C_I :

$$C_I = \frac{< L^i_{kk} >}{< M^i_{kk} >}$$

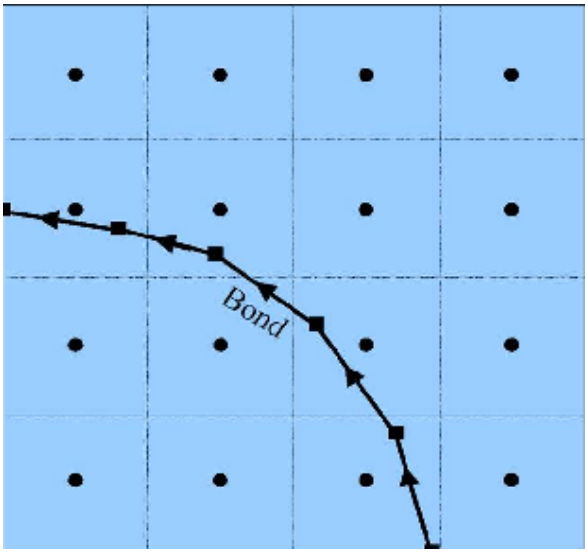

Figure 2.1: 2D Front-tracking on an Eulerian grid (source: Dr. J. Grove)

which can be solved to yield a unique value of C_I.

In a similar manner, the subgrid terms associated with the species mass (turbulent Schmidt number) and energy equation (turbulent Prandtl number) can be modeled.

2.2.1 Front-tracking

In fluid flows, one often encounters situations where there is a sharp discontinuity of some fluid property (density, pressure, etc.). For example, in our study of RMI, there is a large density difference between the two fluids and hence the interface between them represents a density discontinuity. Eulerian numerical schemes without any interface-tracking are very diffusive (lower order schemes) and fail to represent the dynamics at the front correctly [23].

Front-tracking (Fig 2.1) is an adaptive computational method that pro-

vides sharp resolution to a wave front by tracking the interface [6, 18, 14, 11, 16]. The interface being tracked is referred to as the front. A lower dimensional grid is fitted to this front and moves with it. In 2D, the points on the front are connected by piecewise linear segments called bonds.

Two types of updates are needed for the points on the front, the location update to propagate the front and the state update. Every point on the front is assigned two states. These two discontinuous states are the left and the right states. This information is used as the initial condition to solve the Riemann problem at each of these points and update the front.

For the state updates of the interior points (in smooth region), a second order MUSCL is used. For the points close to the front, ghosts cells are used to avoid taking points across the discontinuity [17].
Some of the advantages of using Front-tracking are [14]:

1. It eliminates numerical diffusion that corrupts solution in Eulerian codes without interface-tracking.
2. It gives improved solutions at coarser grids.
3. Shock-contact interactions can be resolved below the grid resolution.
4. There is little effect of grid orientation when using a cartesian grid to compute solutions in curved geomtery.
5. Applicability to complex physics.

Wstar

Wstar is a Python based open-source software to study the stochastic convergence of the solution variables [20]. It is developed by Ryan Kaufman [27] and

is available at `http://www.ams.sunysb.edu/~rkaufman/wstar`. An analogous tool has also been developed in Matlab for circular geometry using the idea of Wstar. This is the software that has been used in our analysis and henceforth, it will simply be referred to as Wstar. The $r\theta-$plane is a natural choice for the supercell given the shape of our domain and placement of the two fluids. It is a post-processing tool that is used to study the convergence properties in a stochastic manner instead of following the traditional pointwise convergence approach. It is based on the idea of a Young measure, which is a space-time dependent probability measure.

The analysis in Wstar is a post-processing step and does not affect the solution in any way. Wstar divides the domain into coarse grid cells (coarser than the mesh size) called supercells. Each supercell contains a number of points in it and values of the solutions associated with these points. The values are binned and from this binned data, a finite approximation to a probability density function (PDF) or a cumulative distribution function (CDF) is formed. Instead of averaging the values, using PDFs/CDFs means that we retain stochastic information, which is a very important aspect of turbulence. Thus, in many ways this is a more appropriate way to analyze convergence for turbulent flows than the pointwise convergence.

The supercell provides a spatial or space-time localization and in this sense, the PDF formed from the supercell is a discrete approximation to a Young measure. The size of the supercell decides how many data points are used to form the PDF/CDF and is very important. As the supercell size is increased, it captures stochastic information better but loses some of its spatial resolution.

The CDFs can be compared, across the grid or across Re numbers, to get the average L1 norm error of the solutions over the entire mixing zone. This value is normalized by dividing it by the total number of cells and difference between the minimum and the maximum values in the range to get a mean error.

In this paper, the joint concentration-temperature CDFs are analyzed across the grid (or Re) to study the associated L1 norm error and mesh convergence. As expected, the error is bigger for the smaller supercell but improves as one increases the supercell size. This reduction in error can be attributed to the bigger sample size of the data.

The two important parameters that affect the error in this analysis are:

- supercell size
- number of bins

Rather than choosing them randomly, we make an informed decision based on the nature of the data. We use beta distribution on concentration data to make these decisions. The results from this analysis are discussed in the upcoming chapters.

Chapter 3

Mix in High Re Limit and Stochastic Convergence

Reprinted from High Energy Density Physics, Vol number 9, J. Melvin, P. Rao, R. Kaufman, H. Lim, Y. Yu, J. Glimm and D.H. Sharp, Atomic scale mixing for inertial confinement fusion associated hydro instabilities, 288-296, 2013, with permission from Elsevier.

3.1 Simulation Setup

We study RMI in 2D imploding circular geometry (3.1) inspired from the ICF design. The governing equations are compressible Navier-Stokes with reflection boundary. The grid information as well as some of the initial parameters are:

- $Sc = 1$, where $Sc = \frac{\nu}{D}$
- $Pr = 10^{-4}$, where $Pr = \frac{\nu}{\alpha}$

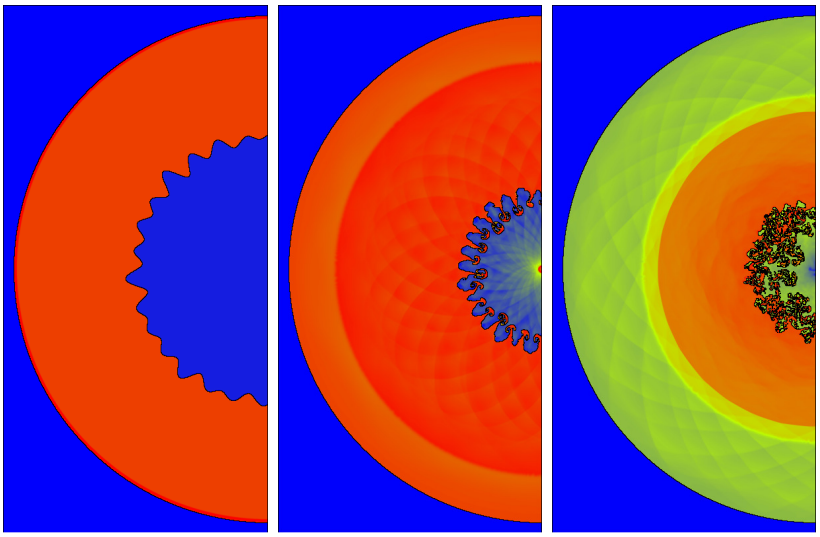

Figure 3.1: RMI from our simulations. **Left:** Initial time **Center:** After shock **Right:** After reshock

- $A = 0.6$, where $A = \frac{\rho_H - \rho_L}{\rho_H + \rho_L}$
- $Mach = 2$
- Grid Size
  - 200×400 (1250 μ)- I (double coarse, DC)
  - 400×800 (625 μ)- II (coarse, C)
  - 80×1600 (312.5 μ)- III (medium, M)
  - 1600×3200 (156.25 μ)- IV (fine, F)
- $Re = 3.5 \times 10^4, 6 \times 10^5, 6 \times 10^6, 6 \times 10^7, "\infty"$

In a high Re shock driven flow, molecules ionize and exhibit strong thermal coupling to the electron and radiation fields. For this reason, we consider a

fluid with a plasma-like highly heat conductive Prandtl number $Pr = 10^{-4}$ and a Schmidt number $Sc = 1$. These are laminar transport values. The primary purpose of this paper is to examine the corresponding turbulent transport coefficients. We define the high Re limit as molecular viscosity $\nu \to 0$ with fixed values for Sc and Pr. This theoretical definition yields a uniquely specified theoretical limit.

To complete the specification of fluid transport input parameters, we set the (molecular level) isotropic viscosity to zero and introduce a Re dependent shear (anisotropic) kinematic viscosity $\nu = 5.13 \times 10^{-4}$ m^2/sec for $Re = 6 \times 10^5$. We use inverse scaling of ν with Re for other Reynolds numbers. The levels of mixing and the value of Re achieved in ICF processes is a subject of ongoing research, outside of the scope of this study.

We study a series of mesh levels (Δx from 6.25×10^{-4}m to 1.56×10^{-4}m) and Re values from $Re = 3.5 \times 10^4$ to a finite mesh approximation of $Re \approx \infty$ (obtained by setting the molecular viscosity to 0). We mention previous studies of the same problem [34, 40]. The numerical study is based on the front tracking code FronTier [12, 2] enhanced with an LES turbulence model (Germano and Moin's dynamic subgrid model [13, 44]) and dynamic subgrid scale (SGS) terms. The tracking reduces excess numerical species diffusion.

3.2 Stochastic Convergence of Turbulent Solutions

3.2.1 Convergence Analysis Method

Our convergence strategy is stochastic in nature and it is algorithmically a post processing method. Therefore, it does not modify the simulation itself. The authors are not aware of a similar construction employed by others for analysis of numerical solutions of partial differential equations.

We retain solution stochastic information (fluctuations and their PDFs) through a coarse graining strategy where we organize the mesh cells into a coarse grained mesh of supercells. Please see Fig. 3.2 to see what a supercell looks like. All solution values in a single supercell are combined to form a finite approximation to a probability density function (PDF) or its indefinite integral, the cumulative distribution function (CDF). In this construction, the coarse grained supercell provides the (reduced) spatial or space-time localization. Such a construction is a discrete approximation to a space-time dependent probability measure, also known as a Young Measure.

Whether assessing convergence or the effects of variation of physical parameters, we are comparing solutions. The difference between solutions is expressed, in each supercell, as the difference between two coarse grain localized CDFs. In each supercell, the solution data is discretized into bins based on the solution variables under study. From this binned data, we create an empirical PDF or CDF. The norm of the difference is defined first through an L_1 norm over the solution state variables, i.e., of the L_1 norm difference of the

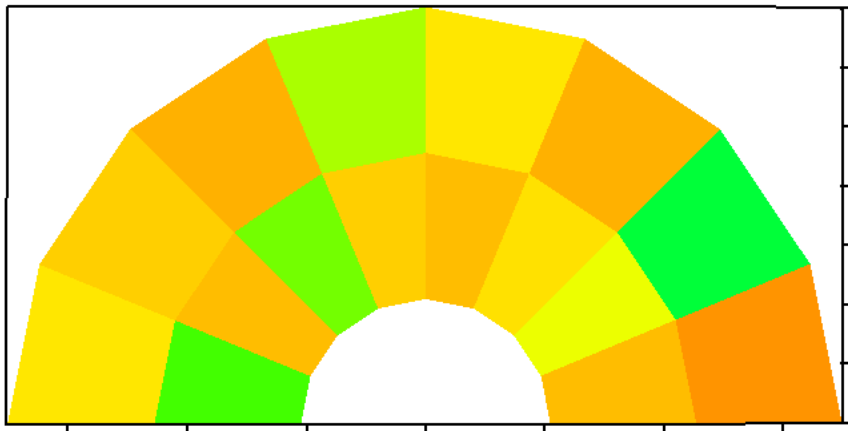

Figure 3.2: The colored blocks represent the supercell.

CDFs over the space of bins, and normalized by division by the number of bins, and by division by the difference between the maximum and minimum solution values over the domain. Such a norm difference is defined as a function defined on each supercell. A spatial mean (an L_1 norm over all supercells in the domain, divided by the total supercell area in the domain) completes the definition of the norm of the difference of the CDFs. This strategy for convergence has been developed in previous papers [25, 26, 27].

3.2.2 Supercell and Bin Sizing

We now examine choices for bin and supercell size. The main focus of this paper is on the distribution of temperature and concentration values. In this section, we focus on the concentration marginal PDF, as its convergence is more sensitive. A common model for concentration PDFs is the beta distribution, which we use as a surrogate to analyze supercell and bin selections.

For a mass fraction x, the beta distribution has a PDF

$$x^{\alpha-1}(1-x)^{\beta-1}/B(\alpha,\beta) \tag{3.1}$$

with the normalizing constant

$$B(\alpha,\beta)=\int_0^1 u^{(\alpha-1)}(1-u)^{(\beta-1)}du \tag{3.2}$$

This distribution is completely characterized by its mean μ and variance σ, related to α and β by the formulas

$$\alpha=(\mu^2-\mu^3-\mu\sigma^2)/\sigma^2 \tag{3.3}$$

and

$$\beta=(\mu-2\mu^2+\mu^3-\sigma^2+\mu\sigma^2)/\sigma^2 \tag{3.4}$$

In Fig. 3.3 left, we plot the histogram of all concentration values taken from the middle 80% of the mixing zone at $t = 90$, shortly after reshock, for $Re = 6\times10^7$. In this paper, we focus our analysis on the middle 80% of the mixing zone, in order to reduce the edge effects of the mixing zone. We determine the parameters $\alpha = 0.360$ and $\beta = 0.286$ from this data and plot the corresponding beta distribution PDF. In Fig. 3.3 right, we compare the empirical (solid curve) and theoretical (dotted curve) CDFs of these two distributions. The L_1 difference, an assessment of the model error, is 0.074.

The supercell size regulates the amount of stochastic information captured in this description and the level of spatial resolution lost in the process. In

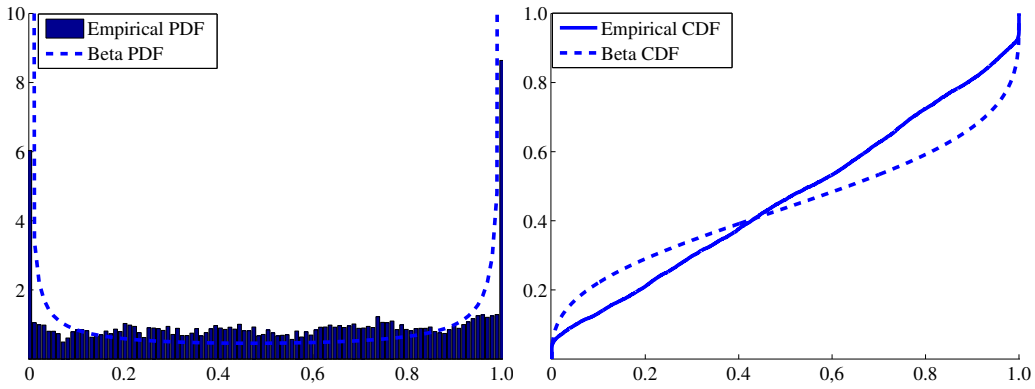

Figure 3.3: Left. Histogram for concentration data and beta distribution with the parameters $\alpha = 0.360, \beta = 0.286$ (dotted curve). Data from $Re = 6 \times 10^7$ coarse grid (II) simulation, $t = 90$. Right. Empirical CDF of the data (solid curve) in middle 80% of the mixing zone from the same simulation as left and beta distribution CDF (dotted curve) with the same parameters α, β.

order to assess mesh convergence issues, we choose supercells large enough that the statistical errors are small relative to the mesh errors. Statistical sampling errors are typically $\mathcal{O}(n^{-1/2})$, where n is the number of cells in a supercell.

We begin with the model beta distribution, determined by the parameters specified above, and take repeated random samples of a fixed size. We analyze each individual sample, by binning the data and forming a sample CDF from the sample data and then taking an L_1 norm between the sample CDF and the beta distribution itself. The L_1 norms are then averaged over the repeated samples to determine an expected mean statistical error that results from the supercell process. In Table 3.1, we display the means and the standard deviations (STDs) of the statistical errors that arise for different sizing of supercells. We can see that upwards of 400 points per supercell are necessary to reduce the statistical error to a value less than 2%. This classifies the trade-

off between supercell sizing (spatial resolution) and accuracy (statistical error) of the method.

Table 3.1: Statistical convergence rates for repeated finite samples of fixed size drawn from the beta distribution, parameters as above. 10 bins used to construct the CDFs.

Sample size	25	100	400	1600
Mean of L_1 norm error for CDFs	0.067	0.033	0.017	0.009
STD of L_1 norm error for CDFs	0.035	0.018	0.009	0.005

To verify the beta distribution as a model for the concentration data, we also repeat the sampling process using the empirical data from the coarse grid (II: 400x800) $Re = 6 \times 10^7$ simulation (used to calculate the beta distribution parameters). In the left frame of Fig. 3.4, we plot the average statistical errors found when comparing the beta distribution to finite samples drawn from it. In the right frame, we plot the average statistical errors found when comparing empirical CDFs of the raw data from the middle 80% of the mixing zone and random samples drawn from this data. Comparing the differences between the theoretical formulation and our specific application, we see roughly unchanged errors between the beta distribution and the empirical distribution, thus justifying the choice of the beta distribution as a surrogate for the concentration PDFs. We also show in Fig. 3.4 insensitivity of the statistical errors to bin size.

From the above analysis, we draw the following conclusions:

1. As a result of the insensitivity of the bin size parameter, we use a bin sizing of 10, per variable, in all analysis performed in this paper.

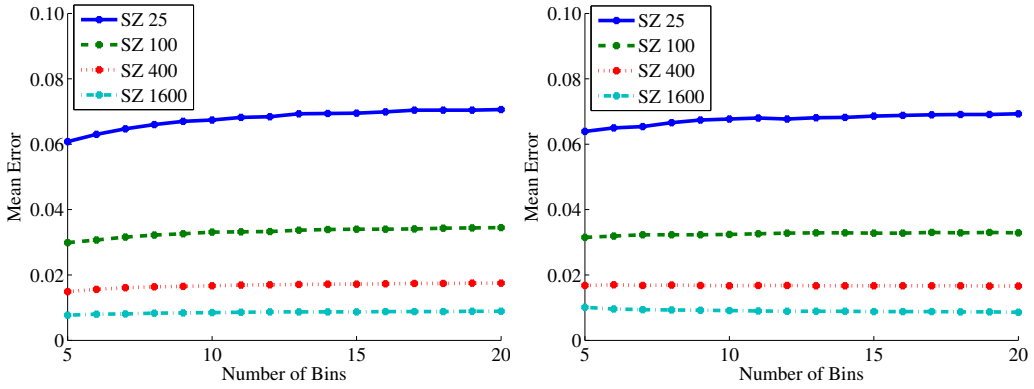

Figure 3.4: L_1 norm of the differences of the concentration CDFs. Left: Repeated finite samples of fixed size, drawn from the beta distribution. Right: The empirical CDF from raw data in the middle 80% of the mixing zone and repeated random samples from this data. The four sample sizes plotted are: 25, 100, 400 and 1600.

2. To obtain statistical errors significantly smaller than mesh errors, we choose to use a supercell size close to 400 datapoints in each supercell on the coarse grid (II: 400x800).

3.3 High Reynolds Number Asymptotics

Here we show, in a purely hydro context, the mildness of the variation introduced in passing from an experimental regime of $Re \approx 3.5 \times 10^4$, well studied experimentally for related Rayleigh-Taylor instabilities, to the ICF regime of $Re \approx 6 \times 10^5$ and larger. This fact supports our V&V proposal of experimental validation at $Re \approx 3.5 \times 10^4$ with verification extrapolation to $Re \approx 6 \times 10^5$.

3.3.1 Convergence of Joint Temperature-Concentration PDFs

We begin by analyzing the convergence properties of the joint temperature-concentration CDFs within the middle 80% of the mixing zone for the $Re = 6\times 10^7$ simulation. L_1 norm convergence of the joint temperature-concentration CDFs was established in [34] for lower Re values, so this value for Re represents an extension of the convergence regime as well as an extension to the case $Pr = 10^{-4}$.

For the supercell gridding, since our mixing zone is radial, we use supercells in r, θ space. Since the data is homogeneous in the θ direction and sensitive to the r direction, discussed in further detail in Sec. 3.3.2, we use 10 supercells in the radial direction and 2 supercells in the angular direction, with a domain consisting only of the datapoints contained in the common mixing zone. With the data structured in x, y space, the r, θ bins have an unequal numbers of points, with an average of 642 points within each supercell of the coarse grid (II: 400x800). The results of this analysis are presented in Table 3.2, from which we see evidence of norm convergence for the CDFs under mesh refinement. The slow convergence rate observed here is consistent with the results of [34], which used an alternate convergence analysis method.

We investigate the dependence of the convergence analysis on the supercell griddings in Table 3.3. We compare a 8x1 (8 in r, 1 in θ), 16x2, 32x4 and 64x8 supercell grid structure. As the supercell size increases (the number of points within a supercell increases), the average norm error decreases. The average number of points in a supercell on the coarse grid is approximately

Table 3.2: L_1 norm convergence of joint CDFs for temperature and concentration (central column) and concentration only (right column) for an RM instability with $Re = 6 \times 10^7$. Meshes: I 200×400, II 400×800, III 800×1600, IV 1600×3200.

Mesh	Temp and Conc	Conc
I-IV	0.092	0.124
II-IV	0.064	0.079
III-IV	0.045	0.058

1600, 400, 100 or 25. We attribute the increase in the norm error to the statistical errors found in Sec. 3.2.2. Consistent with this interpretation is the fact that the increase of error with supercell size is nearly independent of the computational rows. We also note that the slight difference between the 1x1 and 1x8 supercell gridding is due to the convergence of the statistical errors, within a fraction of a percentage point. The supercell size (10x2) selected is a trade-off between statistical accuracy and spatial resolution.

Table 3.3: Variation in the L_1 norm comparison of joint CDFs across mesh levels for different choices of supercells. A coarser supercell mesh corresponds to larger supercells, and improved statistical convergence. All supercell choices are given in radial x angular direction. Meshes as above.

Supercell Grid	1×1	8×1	16×2	32×4	64×8
I-IV	0.079	0.085	0.094	0.102	0.138
II-IV	0.057	0.059	0.065	0.080	0.103
III-IV	0.039	0.041	0.047	0.059	0.076

3.3.2 Spatial Variation of Mix

In Fig. 3.5, we plot the the density over the mixing zone after reshock, for $Re = 6 \times 10^7$.

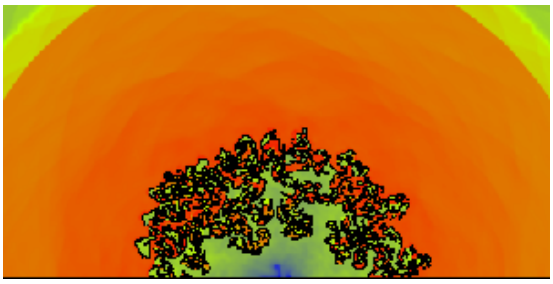

Figure 3.5: Density Plot for $Re = 6 \times 10^7$ after reshock.

The statistics of the PDFs, as they depend on x, y or r, θ, appear uniform in θ but the edge regions for r differ from the central region. The unmixed light fluid (in the mixing zone) is preferentially located near the inner edge and the unmixed heavy fluid is similarly noticeable near the outer edge of the mixing zone.

For $Re = \infty$, we plot the PDFs in four separate zones for the r values, with two central zones and two edge zones, see Fig. 3.6. We observe radial dependence in the mixing properties, with edge zone PDFs containing substantial amounts of unmixed fluids. The outer region has significant unmixed heavy fluid and the inner region significant unmixed light fluid. The central zones, especially the outer central zone, are nearly equi-probable in their distribution, meaning that any mixture fraction is approximately as probable as any other. The inner central zone and the inner edge zone also have significant unmixed light fluid concentrations.

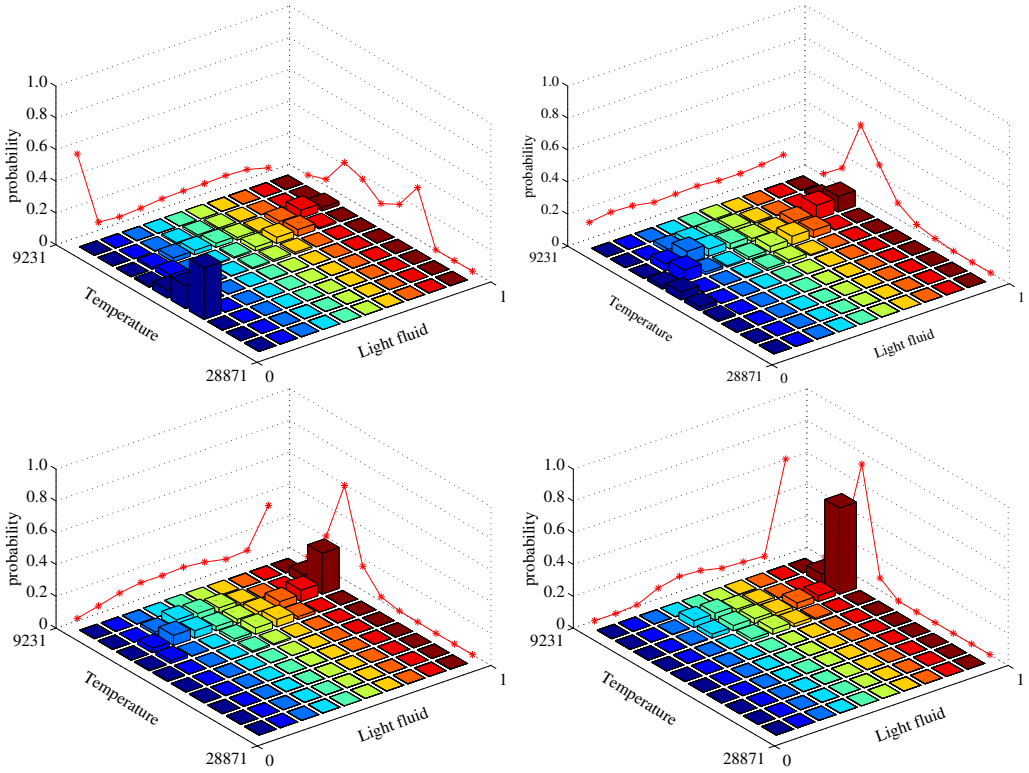

Figure 3.6: PDFs for concentration and temperature for Reynolds number $Re = \infty$ with the variation of PDFs with the radius. Top row, left to right, outer edge r values, and outer central region. Bottom row, left to right, inner central region for r and inner edge region.

We conclude that the temperature and concentration fluctuations are essentially stationary statistically in θ and nearly so in r except near the mixing zone edges. We choose supercells aligned with r, θ coordinate boundaries, large (a) in view of the near stationarity of the statistics and (b) in view of the desire to observe convergence under mesh refinement, and thus to reduce the statistical sampling errors relative to the mesh errors. As with any convergence issue, the resolution will improve as the mesh is refined.

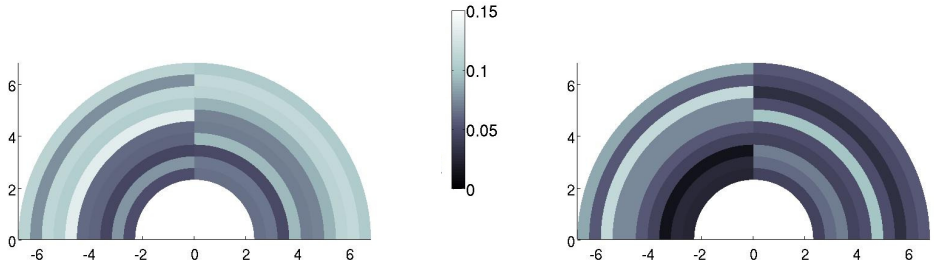

Figure 3.7: Mesh convergence of the concentration CDFs is demonstrated visually, with data from [40]. The left frame compares the coarse to fine mesh; the right frame compares the medium to fine mesh. Colors indicate the level of CDF mesh error in each supercell. Expressing this convergence as an L_1 norm, the order of convergence is 1/2.

3.3.3 *Re* Dependence of Mix

As a main result of this section, we display in Fig. 3.8, the joint PDFs of temperature and concentration for the medium grid (III: 800x1600) $Re = 3.5 \times 10^4$ and for $Re = 6 \times 10^7$. Visually there is minimal difference between the left frame, the experimental regime with Reynolds numbers of 3.5×10^4 and the right frame, beyond the experimentally validated regime at Reynolds number of 6×10^5. We use a supercell grid of 10×2 as above, (approximately 642 points within coarse grid supercell), and consider only the concentration marginals. The *Re* related CDF norm difference of 0.077 is 1.3 times the mesh error of 0.058 (grids III-IV) and thus only marginally observable. See Fig. 3.9.

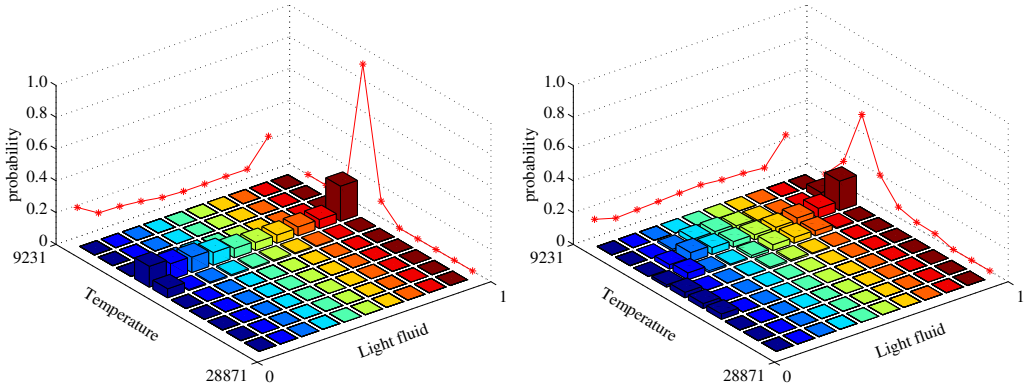

Figure 3.8: Change of Re, $Re = 3.5 \times 10^4$ compared to $Re = 6 \times 10^7$. Left: Joint PDF of temperature and concentration at $Re = 3.5 \times 10^4$. Right: Joint PDF of temperature and concentration at $Re = 6 \times 10^7$.

Figure 3.9: L_1 norm CDF differences between Fig. 3.8, Left, and Right. The L_1 norms result from binning onto supercells, to achieve numerical approximation of the associated CDFs.

3.4 PDF Sensitivity: An $n+1$-parameter family of high Re limits

The n-species compressible Navier-Stokes equations, in the high Re limit, eliminates Re as a parameter. There remain $n+1$ dimensionless fluid transport parameters. The $n-1$ independent Schmidt numbers, the Prandtl number,

and the ratio of two independent viscosities remain to characterize solutions of the Euler equations achieved in the high Re limit process. For LES it is expected that the limit $Re \to \infty$ is independent of the choice of physical transport parameters, if these are fixed and independent of Re in the infinite Re limit process. In this sense the limit is universal relative to molecular fluid transport.

The high Re limit, however, is sensitive to the path taken in the space of dimensionless total (turbulent and molecular) transport coefficients, if these coefficients are given Re dependent values. We demonstrate here sensitivity of the high Re limit to the dimensionless turbulent transport (SGS) terms and their coefficients. For high Re flows, all turbulent Schmidt numbers and the Prandtl number should coincide. There is one parameter to set this common value, which is constrained by validation, i.e., comparison to experiment. A second parameter is the ratio of bulk to shear turbulent viscosities. This important point of solution sensitivity arises in practice as dependence of the solutions upon the algorithms in the high Re limit. The algorithmic dependence of the solution underscores the importance of validation and the relevance within the experimental range of Re, and a mild Re dependent and theoretically based extrapolation, as far as pure hydro issues are concerned, for Re values beyond this range.

From this discussion, we see the importance of turbulence models. If explicit SGS terms are not used, then the fixed point is sensitive to algorithmic details. If a numerical algorithm has significant numerical diffusion (e.g., if tracking is not used), then algorithmic issues will affect the fixed point even

if SGS terms are included. Diffusion, once added numerically, cannot be removed through addition of SGS terms. Thus, we anticipate that numerical algorithms with significant species concentration diffusion will reach only a fraction of the full $n+1$ dimensional parameter space of high Re limits. Mesh refinement short of a DNS simulation will not change this statement.

We justify the assertion of solution nonuniqueness by showing that modifications to the dimensionless turbulent mass diffusion up or down by factors of 10 change the PDFs of the solution variables. We plot in Fig. 3.10, the joint PDFs for concentration and temperature, after an increase and a decrease of turbulent concentration diffusion by factors of 10. We see that the high Re solution is sensitive to the choice of turbulence model. Comparing spatially dependent CDFs obtained by binning solution values into supercells, we find an L_1 norm difference of 0.187 between these two simulations, when using a 10x2 supercell grid and analyzing only the concentration marginal. This L_1 norm difference value is more than three times as large as the mesh error difference for this grid resolution and more than double the normed difference between the simulations with $Re = 3.5 \times 10^4$ compared to $Re = 6 \times 10^7$, presented in Sec. 3.3.3. Thus we conclude that the differences in turbulent mass diffusion are significant and observable, in that they yield CDF differences 3.2 times larger than the statistical and mesh errors.

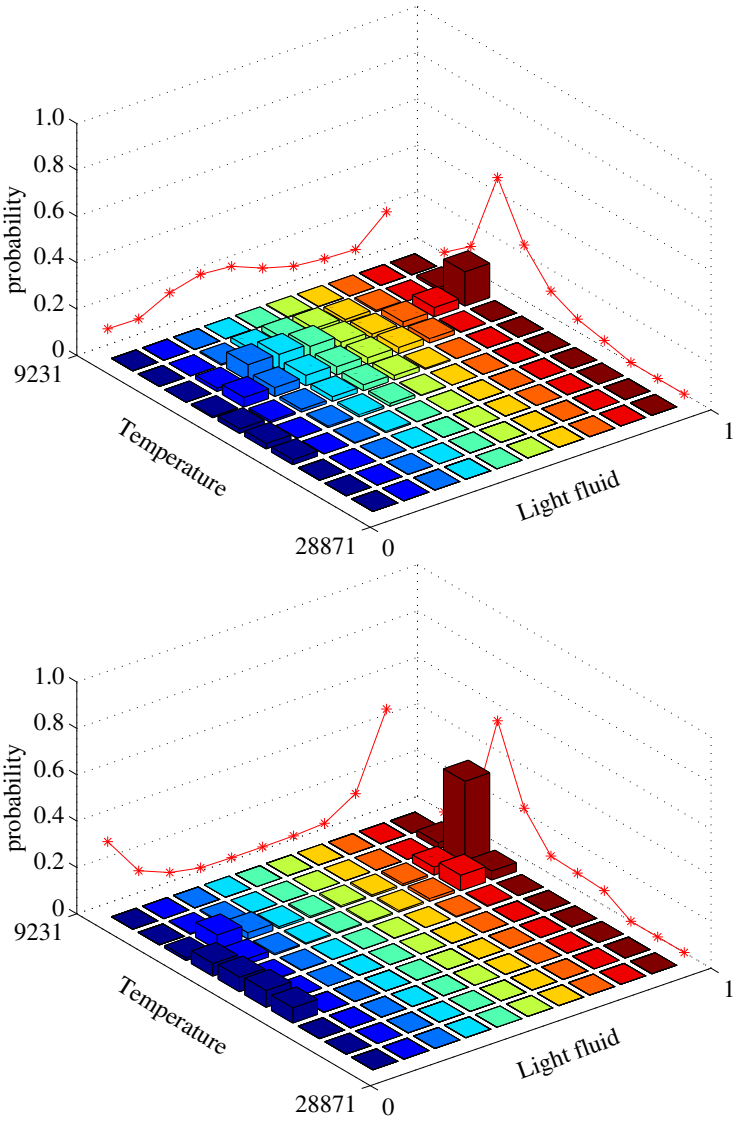

Figure 3.10: PDFs for the joint concentration-temperature distribution for two values of the turbulent transport coefficient for concentration diffusion. Above: 10 times nominal and below: 0.1 times nominal. $Re = 6 \times 10^7$.

Chapter 4

Turbulent Transport Coefficients

Reproduced with permission from ASME paper Turbulent Transport at High Reynolds Numbers in an Inertial Confinement Fusion Context, by J. Melvin, P. Rao, R. Kaufman, H. Lim, Y. Yu, J. Glimm and D. H. Sharp, J. Fluids Eng 136(9), 2014

Mix contributes to numerical solution uncertainty through its dependence on turbulent transport coefficients. These coefficients are a central object of study here, carried out in an Richtmyer-Meshkov unstable circular (2D) geometry suggested by an ICF design. We study a pre-turbulent regime and a fully developed regime.

The former, at times between the first shock passage and reshock, is characterized by mixing in the form of inter-penetrating but coherent fingers and the latter, at times after reshock, has fully developed turbulent structures.

This chapter focuses on the scaling of spatial averages of turbulence coefficients under mesh refinement and under variation of molecular viscosity (i.e., Reynolds number (Re)) [47] . We find that the coefficients scale under mesh refinement with a power of spatial grid spacing derived from the Kolmogorov 2/3 law [29, 30], especially after reshock. We document the dominance of turbulent over molecular transport and convergence of the turbulent transport coefficients in the infinite Re limit. The transport coefficients do not coincide for the pre- and post-reshock flow regimes, with significantly stronger transport coefficients after reshock.

4.1 Scaling Laws for Primitive Equation Quantities

In contrast to 3D turbulence, 2D turbulence has two conserved quantities (energy and enstrophy). The turbulent energy spectrum has two asymptotic scaling ranges, a classical Kolmogorov scaling, $k^{-5/3}$ for intermediate wave numbers k and a specifically 2D scaling law, k^{-3}, driven by enstrophy for large k up to the dissipation range. This theory was presented in the classical arguments of Kraichnan [32] and observed in direct numerical simulations (DNS) of Boffetta [3]. The energy flows in opposite directions under these two cascades, with their associated flow length scales, while the wave number for energy injection marks the division between them.

To examine the scaling properties of the turbulent spectral energy, we plot

in Fig. 4.1 log-log graphs of the turbulent energy spectrum $E(k)$ vs. wave number k for the $Re \approx \infty$ data taken from the finest simulation performed. The spectral analysis depends on a Fourier expansion. In view of the annulus shape of the mixing zone, we analyze with the approximate bounding box for the mixing zone. This results in a wave number normalized by size of the bounding box around the mixing zone (approximately 3/8 of the domain size).

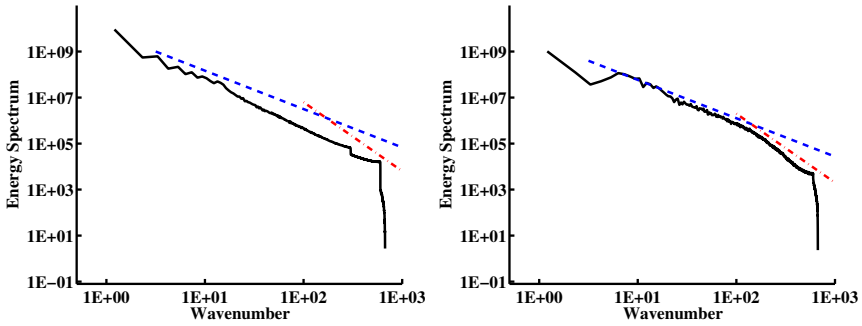

Figure 4.1: Log-Log Energy spectrum plots vs. wavenumber. The reference lines have slopes $k^{-5/3}$ (dashed) and k^{-3} (dash-dot). Left: Pre-reshock. Right: Post-reshock.

The left frame shows data from before reshock and the right frame after reshock. In the left frame, we see a small wave number spectral range for $k^{-5/3}$ and beyond this, a steeper decay less than the theoretical value of -3 but possibly influenced by this effect. The turbulence in the left frame is not yet fully developed at this time and thus the flow features are outside of the scope of Kraichnan's theory. This imperfect scaling can also be observed in Table 4.1. In the right frame (after reshock), Fig. 1 suggests two scaling regimes, an approximate $k^{-5/3}$ and an approximate k^{-3}, which is consistent with Kraichnan's theory. This change in scaling law can also be observed in Table 4.2 with grid levels I-II showing better agreement with each other than

with grid level III.

The Kolmogorov scale for the flows we compute varies from microns or less to 10's of microns at the time of reshock, while the finest mesh considered is $\Delta x = 1.56 \times 10^{-4}$m. The possible k^{-3} scaling regime is visible for only 1/2 an order of magnitude in wave numbers and thus is not definitive, which is in line with comments from [3]. Beyond the differences in physical modeling between [3] and the present work, we do not come close to resolving the Kolmogorov scale. For a compressible calculation, we are not remotely near to DNS. Our finest mesh spacing $\Delta x = 1.56 \times 10^{-4}$m is about a factor of 100 larger than our estimated Kolmogorov scale $\eta \sim L \cdot Re^{-3/4} \sim 2.5 \times 10^{-6}$m, based on the length $L = 5.5 \times 10^{-2}$m (width of the mixing zone) and $Re = 600,000$. This simple analysis suggests many unexplored length scales between the mesh resolution and the Kolmogorov scale, a statement which remains true even for the smallest Re ($Re = 35,000$) considered here.

4.2 Convergence and Variation of Mean Turbulent Transport Coefficients

Assuming that c is mesh convergent, the turbulent transport coefficient χ_{turb} cannot be asymptotically independent of Δx. The strain rate matrix S is assumed to satisfy the Kolmogorov 2/3 law for the local behavior of the two-point correlations, leading to a bound proportional to $\Delta x^{-2/3}$ for each derivative and for each turbulent transport term, and $\Delta x^{-4/3}$ for S factors combined with the gradient, part of M in the flux term. We rewrite the expression for χ_{turb} to

obtain

$$\chi_{\text{turb}} = c\Delta x^{4/3}\left(S\Delta x^{2/3}\right) = c\Delta x^{4/3}S' \ , \tag{4.1}$$

where (4.1) defines S'. Since c is assumed to converge to a finite limit as $\Delta x \to 0$ and S' is assumed to be bounded due to a Kolmogorov type scaling law, we see that χ_{turb} vanishes with Δx at a predicted rate. Remarkably, we observe the same decay rate for all of the turbulent coefficients, even though the decay law is derived from an incompressible, velocity correlation decay (the Kolmogorov 2/3 law for the decay of the velocity correlations). This scaling law is supported for the fully developed turbulence of Table 4.2 and is marginal at best for Table 4.1.

It is clear that these two flow regimes, even in the infinite Re limit, define qualitatively different turbulent flows. Additionally, the post-reshock coefficient mean values show only mild finite Re effects for $Re \geq 3.5 \times 10^4$, while the pre-reshock coefficients transition to (different) nearly Re independent values at higher values of Re. The turbulent thermal and species coefficients are nearly identical to each other.

In Fig. 4.2, we plot fractional mesh errors vs. Re, comparing coarse to fine and medium to fine, for the three dimensionless mean turbulent transport coefficients. The formula used for calculation of this error is $|f - l|/|f|$ where f stands for mean turbulent dimensionless coefficient computed at the finest grid and l stands for the corresponding parameter at medium/coarse grid level. We see that the mesh errors are either small in relative terms or convergent under mesh refinement or both for all values of Re. There is an exception for the turbulent Prandtl number and high Re turbulent Schmidt number,

Table 4.1: Scaled mean turbulent transport coefficients. Mesh I: 400×800, with mesh II doubled and mesh III doubled again. Units are m^2/sec before scaling. Time $t = 5.8 \times 10^{-5}$sec, midway between the first and second shock passage. In the column $Re \approx \infty$, the value is obtained by setting the moleculer viscosity to 0.

Mesh	$Re = 3.5 \times 10^4$	$Re = 6 \times 10^5$	$Re = 6 \times 10^6$	$Re = 6 \times 10^7$	$Re \approx \infty$
$cS' = \nu^a_{\rm turb}/\Delta x^{4/3}$ = scaled anisotropic turbulent viscosity ($m^{2/3}$/sec)					
I	23	24	24	24	24
II	19	20	20	20	21
III	14	14	14	16	15
$cS' = \nu^i_{\rm turb}/\Delta x^{4/3}$ = scaled isotropic turbulent viscosity ($m^{2/3}$/sec)					
I	86	102	95	77	87
II	65	81	75	65	64
III	51	62	60	54	50
$cS' = \mu_{\rm turb}/\Delta x^{4/3}$ scaled species turbulent diffusion ($m^{2/3}$/sec)					
I	37	52	49	38	42
II	29	39	37	29	28
III	21	26	28	23	20
$cS' = \alpha_{\rm turb}/\Delta x^{4/3}$ = scaled turbulent thermal diffusion ($m^{2/3}$/sec)					
I	103	71	44	40	47
II	65	66	42	33	34
III	30	56	41	33	28

especially before reshock, for which further mesh refinement studies would be helpful. Further levels of mesh refinement would allow a deeper examination of 2D turbulence scaling properties for the present problem.

To better understand the high Re asymptotics, we plot in Fig. 4.3 the fractional change $\chi_{\rm turb}(Re)/\chi_{\rm turb}(Re \approx \infty)$ in the mean dimensional transport coefficients vs. Re at the finest grid. The differences between the pre- and post-reshock turbulent flow can be seen by comparing the left frame to the right. We observe a rather mild Re dependence, especially for the fully developed

Table 4.2: Scaled mean turbulent transport coefficients. Meshes and units as in Table 4.1. Time $t = 9.0 \times 10^{-5}$ sec, shortly after the passage of reshock. In the column $Re \approx \infty$, the value is obtained by setting the moleculer viscosity to 0.

Mesh	$Re = 3.5 \times 10^4$	$Re = 6 \times 10^5$	$Re = 6 \times 10^6$	$Re = 6 \times 10^7$	$Re \approx \infty$
$cS' = \nu^a_{\text{turb}}/\Delta x^{4/3}$ = scaled anisotropic turbulent viscosity ($\text{m}^{2/3}$/sec)					
I	44	51	53	47	54
II	48	48	56	58	53
III	57	49	64	64	62
$cS' = \nu^i_{\text{turb}}/\Delta x^{4/3}$ = scaled isotropic turbulent viscosity ($\text{m}^{2/3}$/sec)					
I	214	248	238	214	234
II	222	236	234	232	235
III	253	233	276	277	260
$cS' = \mu_{\text{turb}}/\Delta x^{4/3}$ scaled species turbulent diffusion ($\text{m}^{2/3}$/sec)					
I	112	136	127	127	124
II	115	133	128	122	124
III	133	122	149	148	133
$cS' = \alpha_{\text{turb}}/\Delta x^{4/3}$ = scaled turbulent thermal diffusion ($\text{m}^{2/3}$/sec)					
I	126	163	143	122	132
II	106	181	158	135	145
III	103	174	191	174	149

turbulent flow (right).

To see the dominance of the turbulent transport as a fraction of the total transport, we plot $\chi_{\text{turb}}/\chi_{\text{total}}$ vs. Re in Fig. 4.4. Aside from the Prandtl number, the $Re \approx \infty$ values are nearly reached by $Re = 6 \times 10^6$ for the pre-turbulent flow (left) and by $Re = 6 \times 10^5$ for fully turbulent flow (right). Note the striking qualitative difference between the Prandtl number and the other transport coefficients. Due to the very large level of laminar (molecular) heat conductivity assumed, even the high but finite $Re = 6 \times 10^7$ simulations

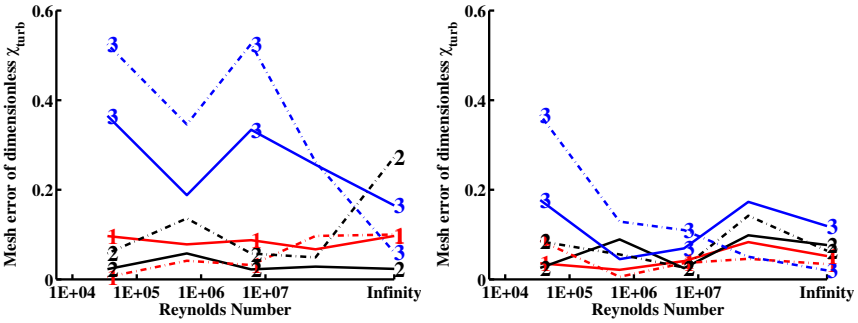

Figure 4.2: Fractional mesh error for dimensionless turbulent transport coefficients, comparing coarse to fine (I-III) and medium to fine (II-III) grids, plotted vs. Re. Left: Before reshock. Right: After reshock. Curves labeled 1, 2, 3 denote inverse isotropic viscosity, Schmidt number and Prandtl number respectively. The dash-dot line denotes the error in the comparison I-III and the soild line denotes the error in the comparison II-III.

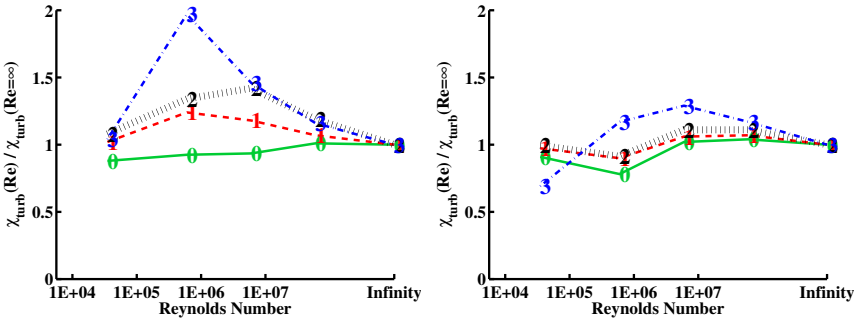

Figure 4.3: Re dependence of mean turbulent transport coefficients for RMI. Fractional variation for each of the four dimensional transport coefficients, plotted as $\chi_{\text{turb}}(Re)/\chi_{\text{turb}}(Re \approx \infty)$ vs. Re, using the finest grid level. Left: Before reshock. Right: After reshock. Curves labeled 0, 1, 2, 3 denote anisotropic viscosity, isotropic viscosity, species diffusivity and thermal diffusivity shown as a fraction of the values of these parameters at $Re \approx \infty$ and plotted vs. the Reynolds number.

display strong finite Reynolds number effects for Pr_{total}. It is for this reason that the Prandtl number curves do not follow the pattern set by the other transport coefficients. The convergence of the total transport to its $Re \approx \infty$

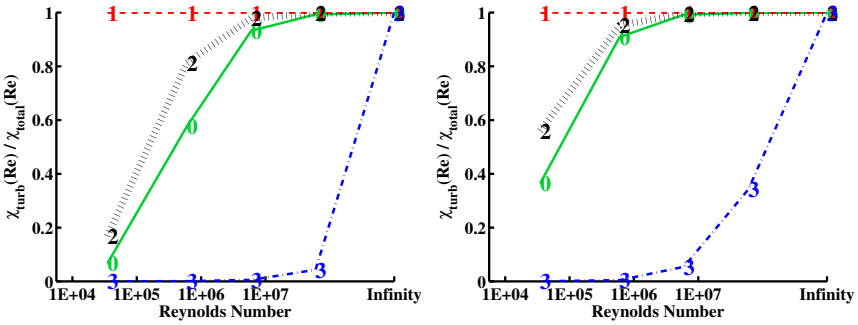

Figure 4.4: Turbulent transport as a fraction of total transport plotted vs. Re for each of four mean transport coefficients, with data taken at the fine grid level. Left: Before reshock. Right: After reshock. Curves labeled 0, 1, 2, 3 denote anisotropic viscosity, isotropic viscosity, species diffusivity and thermal diffusivity respectively, as a fraction of total transport.

asymptotic values is slower for the pre-turbulent (singly shocked) flow than it is for the fully developed turbulent (doubly shocked) flow, a consequence of the smaller values of turbulent transport for the pre-turbulent flow (singly shocked).

Chapter 5

Stochastic Analysis of Mix

The dynamically tracked front serves as the separation between the fluids. Thus, we use it to indicate the level and type of mix. On crossing the front, one switches from one fluid to the other. In this chapter, our goal is to explore the spatial distribution of the mix via analysis of the front.

We begin by selecting a random point on the front and tracing along the ray moving in the normal direction to this point. We stop when we first intersect the front surface along this ray. This new point on the front is called a "front-crossing" or simply a "crossing" and denotes the change of fluid. We will call the length associated with the distance between our original point and this crossing as the "first crossing". Using this new point, we repeat the search along the normal direction and identify the next front point along this new ray. This distance will be referred to as the "second crossing".

We will statistically analyze the lengths of the crossings and determine the relationship between the first and the second crossings. In other words, we

will look at the independence between the two crossings and determine if the overall process is memoryless or not, i.e., if the governing process is Poisson or not. To minimize the sampling errors, we repeat the above procedure for several thousand randomly chosen points on the front.

We analyze the mixing [15] by looking at the distribution of the distances between each crossing.

Following the overall theme of our analysis in earlier chapters, we are mainly going to study two things:

1. mesh comparison of crossings

2. Re comparison of crossings

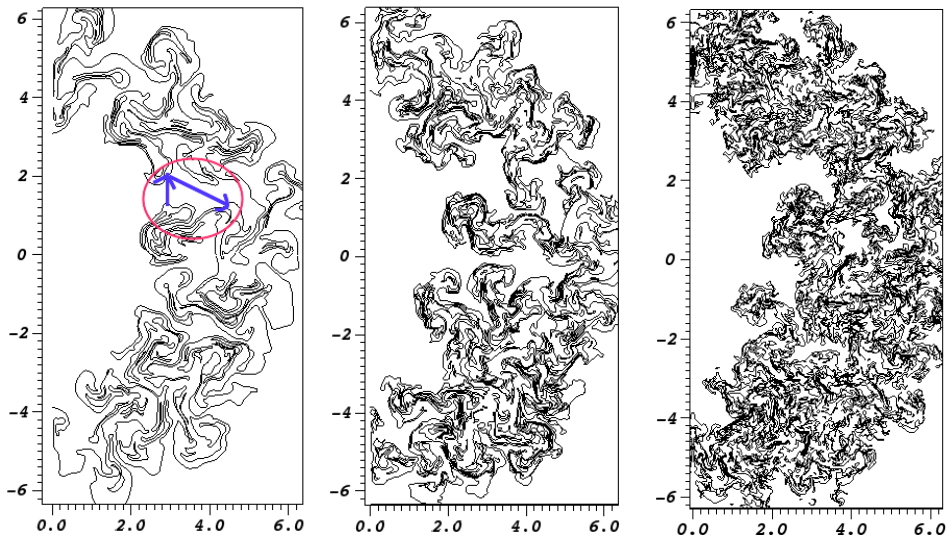

Figure 5.1: **Left to right:** The front depicting the mixing zone at coarse, medium and fine grids for $Re = 6 \times 10^7$. In the far left frame for the coarse grid, the first and the second crossings are encircled and shown by the blue lines.

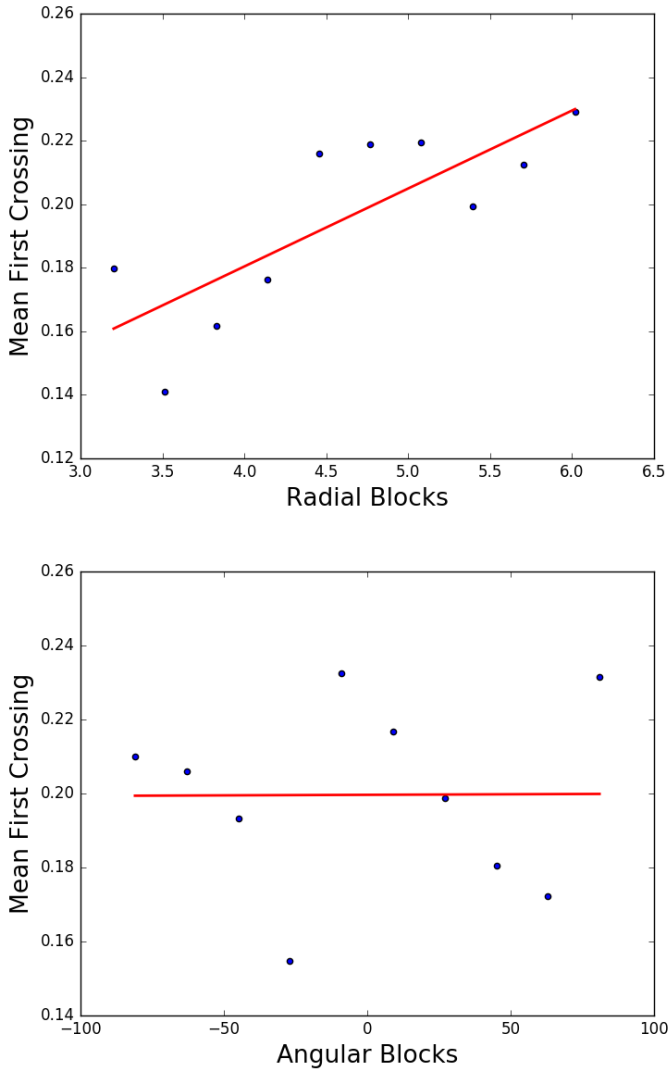

Figure 5.2: Radial dependence (top) and angular dependence (bottom) for $Re = 6 \times 10^7$ at coarse grid.

The individual random variables in a homogeneous Poisson process are independent and follow an exponential distribution with the same rate. Our two random events are:

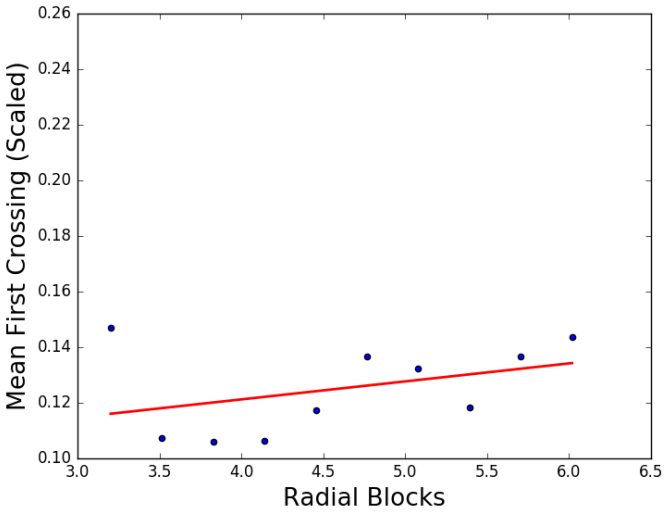

Figure 5.3: Radial dependence removed by scaling the crossings distance for $Re = 6 \times 10^7$ at coarse grid.

1. the distance to the first front crossing from a random point on the front in the normal direction

2. the distance to the second crossing from the first crossing point in the normal direction

We will study if these two random events are independent and exponentially distributed for our data.

5.1 Data Cleaning

To remove the edge effects, we clip the edges of the mixing zone from our analysis and proceed using only the middle two-thirds of the mixing zone. As the mixing zone edges can be slightly different over the three mesh levels, we

study the sub-region of the middle two-thirds region that is common to all three mesh levels. This analysis is carried out on the fully-turbulent late time data, see Fig. 5.1.

The mixing for our problem is anisotropic, which means that it has directional biases. We divide the domain into radial and angular blocks (10 for each) and plot the mean first crossings in Fig. 5.2. In this plot, we document the radial and angular dependence of the crossings using a scatter plot and fitting a regression line to the data. The left frame shows strong radial dependence, while the right frame shows almost no angular dependence.

In order to remove this radial dependence, we fit a line (slope m) to the mean first crossings in the various radial bins and then scale the distance metric using this line (l = mr+c with c=1). After applying this, the radial dependence of the scaled first crossings has become very weak as shown in Fig. 5.3. We will be using this scaled version for our analysis from here on.

5.1.1 Exponential Distribution

The exponential distribution represents a process in which the events occur continuously and independently at a constant average rate.

$$P(x;\lambda) = \lambda e^{-\lambda x}, x \in [0,\infty) \tag{5.1}$$

$$E(X) = \frac{1}{\lambda}, Var(X) = \frac{1}{\lambda^2} \tag{5.2}$$

This distribution can be fully described with just one parameter, namely λ, that is the rate parameter.

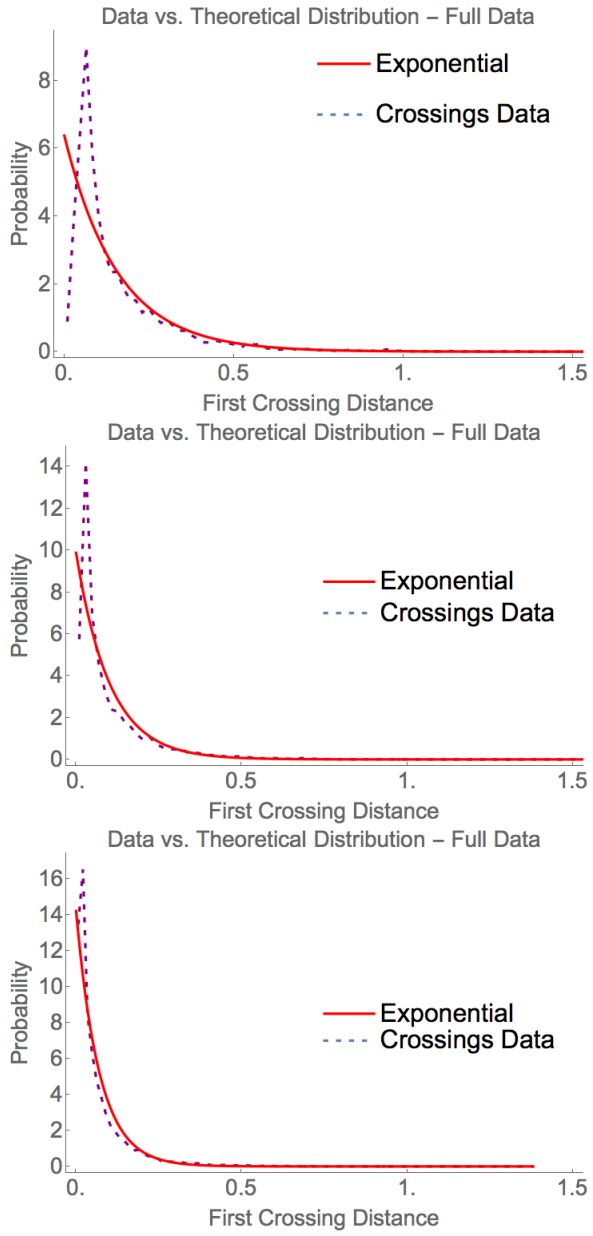

Figure 5.4: **Top to bottom:** PDFs (empirical and exponential) of the first crossings at $Re = 6 \times 10^7$ at coarse (top), medium (center) and fine grids (bottom).

For all three mesh levels, in Fig. 5.4, we take the repeated random samples from the data and compare the empirical probability density function (PDF) generated by binning the data into 100 equally spaced bins with the corresponding theoretical PDF from exponential distribution. The rate parameter λ for the theoretical distribution is obtained by fitting the data to the exponential distribution. The distribution does not seem to be a good fit for the first crossing distances due to the crossings below the size of the grid spacing. We clip the subgrid values from our data because the front has an inherent bias for distances equal to the grid spacing due to the relaxation procedures which use this length scale. For our further analysis, these subgrid values have been truncated from the data.

We plot the empirical vs. theoretical exponential PDFs of the three grid levels with the truncated data and observe a much better agreement (see Fig. 5.5). We also plot the quantile-quantile, or QQ-plots, for our data compared with the true exponential distribution in Fig. 5.6.

5.2 Dependence of the Second Crossing

The first and the second crossings follow exponential distributions individually (see Fig. 5.7), with their rate parameters almost equal, but they are not independent of each other. The second crossing is strongly dependent on the first crossing as shown by the least squares fit to the scatter plot in Fig. 5.8. The correlation coefficient between the first and the second crossings is 0.56.

The dependence of the second crossing on the first crossing shows that even

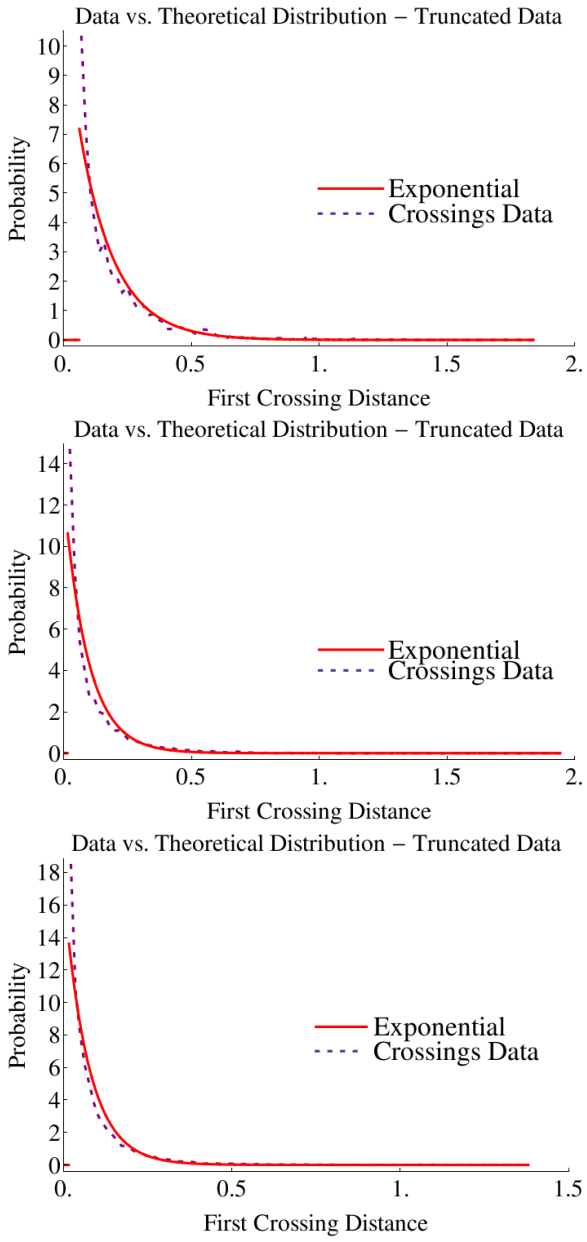

Figure 5.5: **Top:** Coarse. **Center:** Medium. **Bottom:** Fine. This plot shows the empirical PDF and the corresponding theoretical PDF of exponential distribution of the truncated data at the three grid levels for $Re = 6 \times 10^7$.

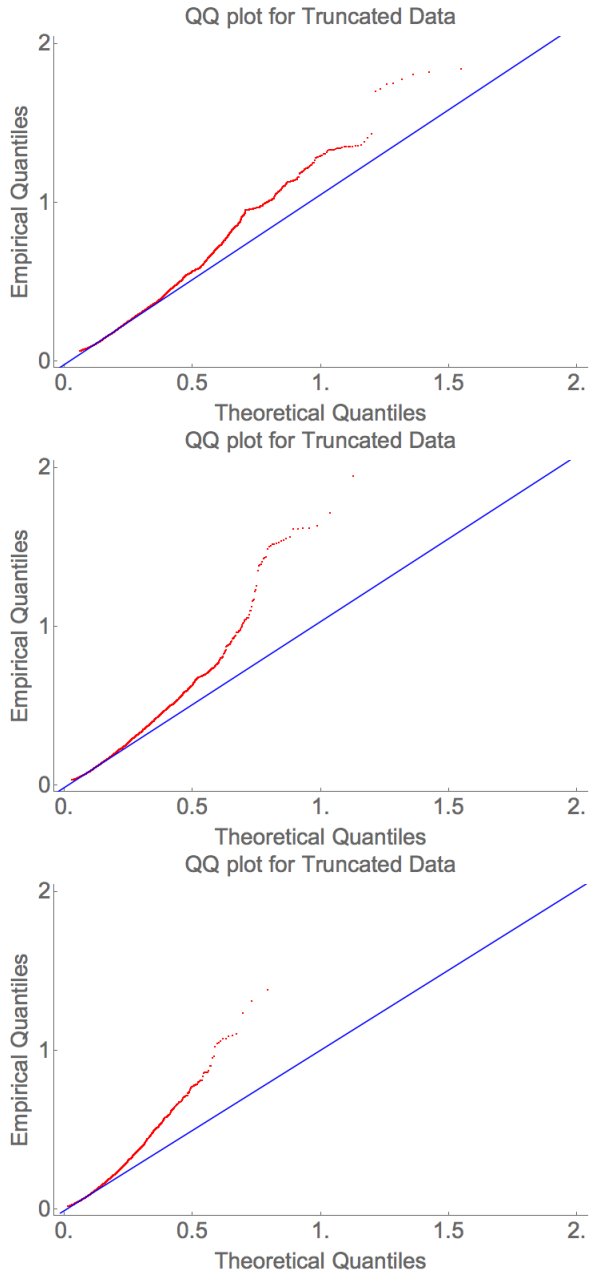

Figure 5.6: QQ-plots of the first crossings at $Re = 6 \times 10^7$ at coarse, medium and fine grids. **Top:** Coarse. **Center** Medium. **Bottom:** Fine.

though the two crossings are exponentially distributed, the underlying process is not Poisson.

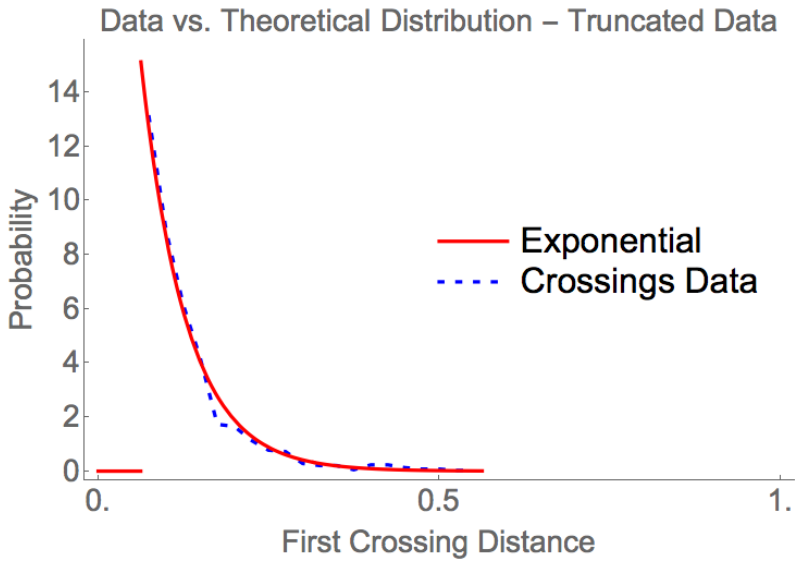

Figure 5.7: Empirical PDF and the theoretical PDF of the second crossings at $Re = 6 \times 10^7$ at coarse.

5.3 Conclusion

We set out to study how the mesh and the Re affect the rate parameters for the exponential distribution. We removed the radial dependence of crossing distance by fitting a line to the mean values from the radial bins and using it to scale the crossings.

Some of the main conclusions from our study are:

1. From table 5.1, we observe that as the mesh is refined, the rate of first crossings increases at a sub-linear rate.

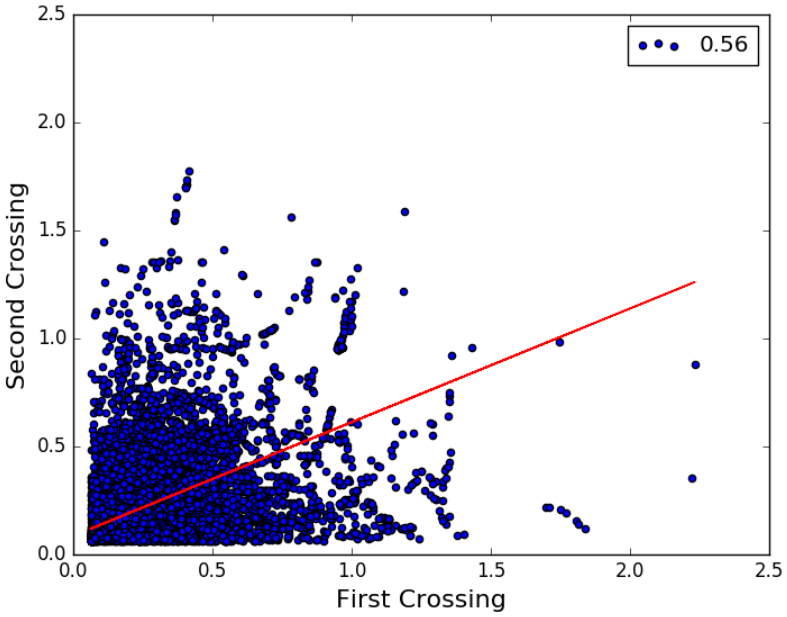

Figure 5.8: Scatter plot of first crossing vs. second crossing and the linear regression line. The second crossing is not independent of the first crossing as demonstrated by the correlation coefficient value of 0.56.

2. In table 5.2, we notice that the rate of the first crossings is almost unchanged between the two Re at the same mesh level.

3. The first and the second crossings have exponential distribution with almost equal rate parameters, λ.

4. The second crossing depends on the first crossing as shown in the scatter plot.

5. Since the first and the second crossings are dependent, the underlying process is not Poisson.

Table 5.1: Mesh dependence (scaled)

$Re = 6 \times 10^7$	Mean	Std. Dev.	λ
Coarse	0.13	0.07	7.99
Medium	0.07	0.04	14.42
Fine	0.04	0.03	23.44

Table 5.2: Re dependence (scaled) at coarse grid

Re	Mean	Std. Dev.	λ
6×10^7	0.13	0.07	7.99
35×10^3	0.14	0.08	7.23

Chapter 6

Summary

The results presented show that in the high Re limit of 2D turbulent mixing, atomic mixing properties are sensitive to models for turbulent transport, and specifically to the numerical algorithm. The limit is demonstrated to be non-unique, supporting the idea that there is an $n+1$-parameter family of fixed points for n-species mixing, with the fixed points labeled by the turbulence model or by the numerical algorithm. Among these non-unique choices, the FT/LES/SGS algorithm selects a unique limit, which agrees well with experiment within the experimental range of Re, in contrast to most ILES simulations, which do not [8].

The turbulent transport coefficients, within this dynamic SGS method, are uniquely specified by theory; the simulations have no tunable parameters. Since zero-parameter numerical models of complex physical phenomena (i.e. fluid turbulence and mixing in the present context) are not so common, we emphasize this aspect of the FT/LES/SGS algorithm. The algorithm is, in

the opinion of the authors, unique among compressible LES simulations in its level of validation (experimental confirmation) for RT experiments. Because of the sensitivity of the atomic level mixture to turbulence models and numerical algorithms, experimental validation is important.

An important conclusion of the present paper is that high Re is only a mild perturbation (in terms of strictly hydro issues) of an experimental regime of $Re \approx 3.5 \times 10^4$, for which there are numerous hydro instability experiments.

The main purpose of this paper is to establish scientific results which support a two step route with experiment and theory supported extrapolation to V&V for high Re simulations.

We explain the main difficulty (non-uniqueness of solutions) and its resolution (dynamic SGS models for LES and front tracking). We review previous work on the experimental comparison step and we present new material relating to the extrapolation step.

In essence, our proposal is that hydro codes should be tested (validated) in the experimental regime and tested numerically (verified) for a parameter free extrapolation from there to the application regime at high Re. Initial conditions for the experimental regime are generally not known, but we have shown that these can be reconstructed from the early time data, with reconstruction uncertainty quantified and an overall effect of $\pm 5\%$ on the value of the RT growth rate α [19].

This is not the first time in which non-uniqueness has been an essential feature of the solutions of time dependent equations, modeled at the inviscid (Euler equation) level. Shock refraction problems, which describe self similar

time dependent solutions, sometimes have multiple solutions. Flame speed is ambiguous when analyzed at the level of the Euler equations, with the ambiguity removed by consideration of the Prandtl number. Detonation waves allow multiple solutions, as weak or strong detonations [7], while some dissipative mechanism often selects the weak detonation. Equations suggested by three phase flow for petroleum reservoirs show non-uniqueness for wave interaction (Riemann) problems [1].

Within the study of turbulence, the sensitivity of solutions to turbulence models is widely understood. However, for turbulence modeling, the analogous resolution of ambiguity (specification of transport coefficients) requires specifying the turbulent transport, exactly the quantity which introduces the ambiguity.

Non-uniqueness of solutions is removed by specification of turbulent (not laminar) transport coefficients, quantities not accessible to direct measurement in a nearly infinite Reynolds number regime, and regarding which there is substantial disagreement. The dynamic subgrid models provide a zero parameter solution. In other words they do select all needed coefficients, and remove all ambiguity. The dynamic subgrid models, combined with front tracking provide excellent agreement with experimental RT data (validation). Here, we claim that validation followed by a mild perturbative verification step reaches the high Re regime. This is an important step towards designing predictive hydro simulations.

We have shown the mesh dependence for the spatially averaged turbulent transport coefficients to be either relatively small or convergent or both, for

all values of Re considered and for the range of length scales (Δx) considered. The notion of pdf convergence depends on an observational length scale for coarse graining simulation values to define a local PDF. Convergence is limited to a range of length scales for which constant scaling behavior is valid. The post-reshock coefficients have a mild Re dependence, while finite Re effects in these coefficients persist to higher Re values for the pre-turbulent, single shocked case. The common post-reshock Kolmogorov 2/3 law scaling among these coefficients is unexplained. The high level of thermal conductivity leads to finite Re effects in the thermal transport even for quite elevated values of Re.

We also analyzed the front crossings using the exponential distribution over a series of mesh and Re. We observed a sub-linear increase in the rate parameter λ as the mesh was refined and almost no change for Re at the same mesh level.

Bibliography

[1] A. Azevedo and D. Marchesin. Multiple viscous solutions for systems of conservation laws. *Trans. Amer. Math. Soc.*, 347:3061–3078, 1995.

[2] W. Bo, X. Liu, J. Glimm, and X. Li. A robust front tracking method: Verification and application to simulation of the primary breakup of a liquid jet. *SIAM J. Sci. Comput.*, 33:1505–1524, 2011.

[3] G. Boffetta. Energy and enstrophy fluxes in the double cascade of two-dimensional turbulence. *J. Fluid Mech*, 589:253–260, 2007.

[4] R. Brouilette. *Rayleigh-Taylor instability in compressible fluids.* PhD thesis, California Institute of Technology, 1989.

[5] M. Brouillette and B. Sturtevant. Richtmyer-Meshkov instability at a continuous interface. In Y. W. Kim, editor, *Current Topics in Shock Waves: 17th International symposium on shock waves and shock tubes*, pages 284–289. AIP, 1990.

[6] I-L. Chern, J. Glimm, O. McBryan, B. Plohr, and S. Yaniv. Front tracking for gas dynamics. *J. Comput. Phys.*, 62:83–110, 1986.

[7] R. Courant and K. Friedrichs. *Supersonic Flow and Shock Waves.* Springer-Verlag, New York, 1967.

[8] G. Dimonte, D. L. Youngs, A. Dimits, S. Weber, M. Marinak, S. Wunsch, C. Garsi, A. Robinson, M. Andrews, P. Ramaprabhu, A. C. Calder, B. Fryxell, J. Bielle, L. Dursi, P. MacNiece, K. Olson, P. Ricker, R. Rosner, F. Timmes, H. Tubo, Y.-N. Young, and M. Zingale. A comparative study of the turbulent Rayleigh-Taylor instability using high-resolution three-dimensional numerical simulations: The Alpha-Group collaboration. *Phys. Fluids*, 16:1668–1693, 2004.

[9] Paul E. Dimotakis. Turbulent mixing. *Annual Review of Fluid Mechanics*, 37(1):329–356, 2005.

[10] R. P. Drake, H. F. Robey, O. A. Hurricane, Y. Zhang, B. A. Remington, J. Knauer, J. Glimm, D. Arnett, J. O. Kane, K. S. Budil, and J. W. Grove. Experiments to produce a hydrodynamically unstable spherically diverging system of relevance to instabilities in supernovae. *Astrophysical Journal*, 564:896–906, 2002.

[11] Jian Du, Brian Fix, James Glimm, Xicheng Jia, Xiaolin Li, Yunhua Li, and Lingling Wu. A simple package for front tracking. *J. Comput. Phys.*, 213:613–628, 2006.

[12] E. George, J. Glimm, J. W. Grove, X.-L. Li, Y.-J. Liu, Z.-L. Xu, and N. Zhao. Simplification, conservation and adaptivity in the front tracking method. In T. Hou and E. Tadmor, editors, *Hyperbolic Problems: Theory, Numerics, Applications*, pages 175–184. Springer Verlag, Berlin and New York, 2003.

[13] M. Germano, U. Piomelli, P. Moin, and W. H. Cabot. A dynamic subgrid scale eddy viscosity model. *Phys. Fluids A*, 3:1760–1765, 1991.

[14] J. Glimm, M. J. Graham, J. W. Grove, X.-L. Li, T. M. Smith, D. Tan, F. Tangerman, and Q. Zhang. Front tracking in two and three dimensions. *Comput. Math. Appl.*, 35(7):1–11, 1998.

[15] J. Glimm, J. W. Grove, X.-L. Li, W. Oh, and D. H. Sharp. A critical analysis of Rayleigh-Taylor growth rates. *J. Comput. Phys.*, 169:652–677, 2001.

[16] J. Glimm, J. W. Grove, X.-L. Li, and D. C. Tan. Robust computational algorithms for dynamic interface tracking in three dimensions. *SIAM J. Sci. Comput.*, 21:2240–2256, 2000.

[17] J. Glimm, J. W. Grove, X.-L. Li, and N. Zhao. Simple front tracking. In G.-Q. Chen and E. DiBenedetto, editors, *Contemporary Mathematics*, volume 238, pages 133–149. Amer. Math. Soc., Providence, RI, 1999.

[18] J. Glimm, W. B. Lindquist, and Q. Zhang. Front tracking, oil reservoirs, engineering problems and mass conservation. In J. Glimm and A. Majda, editors, *Multidimensional Hyperbolic Problems and Computations*, volume 29 of *IMA Volumes in Mathematics and its Applications*, pages 123–139. Springer-Verlag, New York–Heidelberg–Berlin, 1991.

[19] J. Glimm, D. H. Sharp, T. Kaman, and H. Lim. New directions for Rayleigh-Taylor mixing. *Phil. Trans. R. Soc. A*, 371:20120183, 2013. Los

Alamos National Laboratory Preprint LA-UR 11-00423 and Stony Brook University Preprint SUNYSB-AMS-11-01.

[20] J. Glimm, D. H. Sharp, H. Lim, R. Kaufman, and W. Hu. Euler equation existence, non-uniqueness and mesh converged statistics. *Phil. Trans. R. Soc. A*, 373:20140282, 2015. Los Alamos National Laboratory Preprint LA-UR-14-29521 and Stony Brook University Preprint SUNYSB-AMS-14-04.

[21] Xiaoxue Gong, Ying Xu, Vinay Mahadeo, Tulin Kaman, Johan Larsson, and James Glimm. Mesh convergence for turbulent combustion. *Discrete & Continuous Dynamical Systems–Series A*, 16:4383–4402, 2016. Stony Brook University Preprint number SUNYSB-AMS-15-04.

[22] S. W. Haan, D. Lindl, D. A Callahan, D. S. Clark, J. D. Salmonson, B. A. Hammel, L. J. Atherton, R. C. Cook, M. J. Edwards, S. Glenzer, A. V. Hamza, S. P. Hatchett, M. C. Herrman, D. E. Hinkel, Ho D, D, H. Huang, O. S. Jones, J. Kline, G. Kyrala, O. L. Landen, B. J. MacGowan, M. M. Marinak, D. D. Meyerhofer, J. L. Milovich, K. A. Moreno, E. I. Moses, D. H. Munro, A. Nikroo, R. E. Olson, K. Peterson, S. M. Pollaine, J. E. Ralph, H. F. Robey, B. K. Spears, P. T. Springer, L. J. Suter, C. A. Thomas, R. P. Town, R. Vesey, S. V. Weber, H. L. Wilkins, and D. C. Wilson. Point design targets, specifications, and requirements for the 2010 ignition campaign on the national ignition facility. *Phys. Plasmas*, 18:051001, 2011.

[23] R. L. Holmes. *A Numerical Investigation of the Richtmyer-Meshkov Instability Using Front Tracking*. PhD thesis, State Univ. of New York at Stony Brook, 1994.

[24] Wenlin Hu. *Statistical Moments in Variable-Density Incompressible Mixing Flows*. PhD thesis, Stony Brook University, 2015.

[25] T. Kaman, R. Kaufman, J. Glimm, and D. H. Sharp. Uncertainty quantification for turbulent mixing flows: Rayleigh-Taylor instability. In A. Dienstfrey and R. Boisvert, editors, *Uncertainty Quantification in Scientific Computing*, volume 377 of *IFIP Advances in Information and Communication Technology*, pages 212–225. Springer, 2012. Stony Brook University Preprint number SUNYSB-AMS-11-08.

[26] T. Kaman, J. Melvin, P. Rao, R. Kaufman, H. Lim, Y. Yu, J. Glimm, and D. H. Sharp. Recent progress in turbulent mixing. *Physica Scripta*,

page 014051, 2013. Stony Brook University Preprint number SUNYSB-AMS-11-09. Los Alamos National Laboratory preprint LA-UR 11-06770.

[27] Ryan Kaufman, Tulin Kaman, Yan Yu, and James Glimm. Stochastic convergence and the software tool W*. In *Proceeding Book of International Conference to honour Professor E.F. Toro*, pages 37–41. CRC, Taylor and Francis Group, 2012. Stony Brook University Preprint number SUNYSB-AMS-11-10.

[28] Richard I. Klein, Kimberly S. Budil, Theodore S. Perry, and David R. Bach. Interaction of supernova remnants with interstellar clouds: From the nova laser to the galaxy. *The Astrophysical Journal Supplement Series*, 127(2):379, 2000.

[29] A. N. Kolmogorov. Local structure of turbulence in incompressible viscous fluid for very large Reynolds number. *Doklady Akad. Nauk. SSSR*, 30:299–3031, 1941.

[30] A. N. Kolmogorov. A refinement of previous hypotheses concerning the local structure of turbulence in a viscous incompressible fluid at high reynolds number. *J. Fluid Mechanics*, 13:82–85, 1962.

[31] K. A. Kowalsky, D. R. Marantz, M. F. Smith, and W. L. Oberkampf. HVOF: Particle, flame diagnostics and coating characteristics. In *Thermal Spray and Applications, Proceedings of the Third National Thermal Spray Conference, Long Beach, CA*. 1990.

[32] R. H. Kraichnan. Inertial ranges in two-dimensional turbulence. *J. Fluid Mech.*, 16:1417–1423, 1967.

[33] M. Lesieur and O. Metais. New trends in large eddy simulations of turbulence. *Ann. Rev. Fluid Mech.*, 28:45–82, 1996.

[34] H. Lim, Y. Yu, J. Glimm, X. L. Li, and D. H. Sharp. Subgrid models for mass and thermal diffusion in turbulent mixing. *Physica Scripta*, T142:014062, 2010. Stony Brook Preprint SUNYSB-AMS-08-07 and Los Alamos National Laboratory Preprint LA-UR 08-07725.

[35] John D. Lindl. *Inertial Confinement Fusion*. Springer-Verlag, New York, 1998.

[36] John D. Lindl, Peter Amendt, Richard L. Berger, S. Gail Glendinning, Seigfried H. Glazer, Steven H. Haan, Robert L Kauffman, Otto L. Linden,

and Laurence J. Suter. The physics basis for ignition using indirect-drive targets on the national ignition facility. *Phys. Plasmas*, 11:339–491, 2004.

[37] Lord Rayleigh. Investigation of the character of the equilibrium of an incompressible heavy fluid of variable density. In *Scientific Papers*, volume II, page 200. Cambridge Univ. Press, Cambridge, England, 1900.

[38] T. Ma. *Large-eddy simulation of variable density flows*. PhD thesis, University of Maryland, 2006.

[39] J. Melvin, H. Lim, V. Rana, B. Cheng, J. Glimm, D. H. Sharp, and D. C. Wilson. Sensitivity of inertial confinement fusion hot spot properties to the deuterium-tritium fuel adiabat. *Physics of Plasmas*, 22:022708, 2015.

[40] J. Melvin, P. Rao, R. Kaufman, H. Lim, Y. Yu, J. Glimm, and D. H. Sharp. Atomic scale mixing for inertial confinement fusion associated hydro instabilities. *High Energy Density Physics*, 9:288–298, 2013. Stony Brook University Preprint SUNYSB-AMS-12-01 and Los Alamos National Laboratory Preprint LA-UR 12-21555.

[41] J. Melvin, P. Rao, R. Kaufman, H. Lim, Y.Yu, J. Glimm, and D. H. Sharp. Turbulent transport at high reynolds numbers in an ICF context. *J. Fluids Eng.*, 136(9)(Stony Brook University Preprint Number SUNYSB-AMS-13-02, Los Alamos National Lab LAUR Number LA-UR-13-20765):091206, 2014.

[42] E. E. Meshkov. Instability of a shock wave accelerated interface between two gases. *NASA Tech. Trans.*, F-13:074, 1970.

[43] Karnig O. Mikaelian. Turbulent mixing generated by rayleigh-taylor and richtmyer-meshkov instabilities. *Physica D: Nonlinear Phenomena*, 36(3):343 – 357, 1989.

[44] P. Moin, K. Squires, W. Cabot, and S. Lee. A dynamic subgrid-scale model for compressible turbulence and scalar transport. *Phys. Fluids A*, 3:2746–2757, 1991.

[45] William L. Oberkampf and Timothy G. Trucano. Verification and validation in computational fluid dynamics. *Progress in Aerospace Sciences*, 38(3):209 – 272, 2002.

[46] Stephen B Pope. Ten questions concerning the large-eddy simulation of turbulent flows. *New Journal of Physics*, 6(1):35, 2004.

[47] P. Rao, J. Melvin, W. Hu, R. Kaufman, H. Lim, and J. Glimm. Predictive simulations for problems with solution non-uniqueness. In *11th World Congress on Computational Mechanics (WCCM XI)*, 2014. Stony Brook University Preprint SUNYSB-AMS-14-01.

[48] L. Rayleigh. On the stability of jets. *Proc Lond Math Soc*, 10:4–13, 1878.

[49] R. D. Richtmyer. Taylor instability in shock acceleration of compressible fluids. *Comm. Pure Appl. Math.*, 13:297–319, 1960.

[50] D. D. Ryutov, R. P. Drake, and J. Kane et al. Similarity criteria for the laboratory simulation of supernova hydrodynamics. *ApJ*, 518:821–832, 1999.

[51] D. H. Sharp. An overview of Rayleigh-Taylor instability. *Physica D*, 12:3–18, 1984.

[52] J. Smagorinsky. General circulation experiments with the primitive equations. *Mon. Weather Rev.*, 91:99–165, 1963.

[53] D. L. Youngs. Application of MILES to Rayleigh-Taylor and Richtmyer-Meshkov mixing. Technical Report 4102, American Institute of Aeronautics and Astronautics, 2003. Presented at the 16th AIAA Computational Fluid Dynamics Conference.